Monthly Notices
of the
ROYAL ASTRONOMICAL SOCIETY

MNRAS **487,** 5593–5609 (2019)
Advance Access publication 2019 June 12

doi:10.1093/mnras/stz1631

Inquiring into the nature of the Abell 2667 brightest cluster galaxy: physical properties from MUSE

E. Iani ,[1,2★] G. Rodighiero,[1,3★] J. Fritz,[4] G. Cresci,[5] C. Mancini,[1,3] P. Tozzi,[5] L. Rodríguez-Muñoz ,[1] P. Rosati,[6] G. B. Caminha,[7] A. Zanella,[2] S. Berta,[8] P. Cassata,[1] A. Concas,[9] A. Enia,[1] D. Fadda,[10] A. Franceschini,[1] A. Liu,[5] A. Mercurio,[11] L. Morselli,[9] P. G. Pérez-González,[12,13] P. Popesso,[9] G. Sabatini,[14,15,16] J. Vernet [2] and R. J. van Weeren[17]

Affiliations are listed at the end of the paper

Accepted 2019 June 10. Received 2019 June 6; in original form 2019 March 11

ABSTRACT

Based on *HST* and MUSE data, we probe the stellar and gas properties (i.e. kinematics, stellar mass, star formation rate) of the radio-loud brightest cluster galaxy (BCG) located at the centre of the X-ray-luminous cool-core cluster Abell 2667 ($z = 0.2343$). The bi-dimensional modelling of the BCG surface brightness profile reveals the presence of a complex system of substructures extending all around the galaxy. Clumps of different size and shape plunged into a more diffuse component constitute these substructures, whose intense 'blue' optical colour hints at the presence of a young stellar population. Our results depict the BCG as a massive ($M_\star \simeq 1.38 \times 10^{11}\,\mathrm{M}_\odot$) dispersion-supported spheroid ($\Delta v_\star \leq 150\,\mathrm{km\,s^{-1}}$, $\sigma_0 \sim 216\,\mathrm{km\,s^{-1}}$) hosting an active supermassive black hole ($M_{\mathrm{SMBH}} \simeq 3.8 \times 10^9\,\mathrm{M}_\odot$) whose optical features are typical of low-ionization nuclear emission line regions. Although the velocity pattern of the stars in the BCG is irregular, the stellar kinematics in the regions of the clumps show a positive velocity of $\sim$100 km s^{-1}, similarly to the gas component. An analysis of the mechanism giving rise to the observed lines in the clumps through empirical diagnostic diagrams points out that the emission is *composite*, suggesting contribution from both star formation and an active galactic nucleus. We conclude our analysis describing how scenarios of both *chaotic cold accretion* and *merging* with a gas-rich disc galaxy can efficaciously explain the phenomena the BCG is undergoing.

Key words: galaxies: active – galaxies: clusters: general – galaxies: clusters: intracluster medium – galaxies: elliptical and lenticular, cD – galaxies: evolution – galaxies: kinematics and dynamics.

1 INTRODUCTION

Brightest cluster galaxies (BCGs) are the largest, most massive and optically luminous galaxies in the Universe. They sit almost at rest at the bottom of clusters' potential wells and close to the peak of the thermal X-ray emission originated by the hydrostatic cooling of the hot (10^7–10^8 K) intracluster medium (ICM). Based on their optical morphology and their 'red' optical/near-infrared (NIR) colours, which suggest relatively old stellar populations and little ongoing star formation activity (e.g. Dubinski 1998; Tonini et al. 2012; Bai et al. 2014; Zhao, Aragón-Salamanca & Conselice 2015), BCGs are typically classified as giant ellipticals or cD galaxies. However, they distinguish themselves from cluster ellipticals because of different surface brightness profiles (i.e. shallower surface brightness and higher central velocity dispersion; e.g. Oemler 1976; Schombert 1986; Dubinski 1998) and larger masses and luminosities (BCGs are often found to be a few times brighter than the second and third brightest galaxies in a cluster). Additionally, BCGs have been shown to lie off the standard scaling relations of early-type galaxies (e.g. Bernardi 2007; Lauer et al. 2007; Von Der Linden et al. 2007; Bernardi 2009) with luminosities (or stellar masses) significantly above the prediction of the standard Faber–Jackson relation (e.g. Lauer et al. 2014). For these reasons, BCGs do not appear to represent the high-mass end of the luminosity function of either cluster ellipticals (e.g. Tremaine & Richstone 1977; Dressler 1984) or bright galaxies in general (Bernstein & Bhavsar 2001), defining in this way a galaxy class on their own

★ E-mail: edoardo.iani@phd.unipd.it (EI); giulia.rodighiero@unipd.it (GR)

© 2019 The Author(s)
Published by Oxford University Press on behalf of the Royal Astronomical Society

Downloaded from https://academic.oup.com/mnras/article/487/4/5593/5514359 by guest on 26 November 2020

(e.g. Dressler 1984; De Lucia & Blaizot 2007; Bonaventura et al. 2017).

As a result of their peculiar location within clusters, BCGs can show exceptional properties over the whole electromagnetic spectrum. Hence, a profusion of studies probing their nature has been carried out from X-rays to the radio domain (e.g. Burke, Collins & Mann 2000; Stott et al. 2010; Lidman et al. 2012; Dutson et al. 2014; Webb et al. 2015). The results of these works show that BCGs with bright mid- and far-infrared emission likely host star formation as well as active galactic nuclei (AGNs). In this case, the infrared emission is the consequence of the absorption and re-emission by dust of ultraviolet (UV) light generated by either young stars or the hard radiation field of AGNs. Both ongoing star formation and AGN activity induce BCGs to be detected in the radio domain. In this regard, studies on the fractional radio luminosity function of elliptical galaxies (e.g. Auriemma et al. 1977; Ledlow & Owen 1996; Mauch & Sadler 2007; Bardelli et al. 2010) have shown that the probability of a galaxy hosting a radio-loud source strictly depends on its visual magnitude. Specifically, for a given galaxy radio power, the radio luminosity function increases depending on the galaxy mass and the crowdedness of its environment. Therefore, BCGs are by definition the galaxies with the highest probability of hosting an AGN (e.g. Best et al. 2007; Von Der Linden et al. 2007; Mittal et al. 2009). Indeed, a radio survey of BCGs residing in CLASH (i.e. the Cluster Lensing And Supernova survey with *Hubble*; Postman et al. 2012) clusters show that BCGs frequently host a radio galaxy, with the radio emission at least 10 times more powerful than expected from measured star formation (e.g. Yu et al. 2018). If the AGN is sufficiently unobscured and radiatively efficient, it is detected in the X-rays (e.g. Yang et al. 2018) with its optical counterpart featuring emission line ratios typical of low-ionization nuclear emission regions (LINERs; e.g. Heckman et al. 1989; Crawford et al. 1999). Ultimately, evidence of a multiphase ICM surrounding BCG cores has been unveiled by the X-ray (e.g. Fabian 1994), in the UV via the O VI line (Bregman, Miller & Irwin 2001), the extended Ly α (Hu 1992), and far-UV continuum (e.g. O'Dea et al. 2004) emissions, in the optical, predominantly via the H α + [N II] emission (e.g. Heckman et al. 1989; Crawford et al. 1999; McDonald 2011), and in the near-IR and mid-IR via the roto-vibrational (Donahue et al. 2000; Edge et al. 2002) and pure rotational H_2 lines (Egami et al. 2006; Johnstone et al. 2007; Donahue et al. 2011).

In the last decades, a plethora of studies have investigated both observationally and theoretically the mechanisms at the origin of BCG formation. The results obtained in these works invoke either *cooling flows* (Silk 1976; Cowie & Binney 1977; Fabian & Nulsen 1977; Fabian 1994) or *galactic cannibalism* (Ostriker & Tremaine 1975; White 1976; Malumuth & Richstone 1984; Merritt 1985) to explain the stellar mass growth of these galaxies. Cooling flows are streams of subsonic pressure-driven cold ICM (e.g. O'Dea et al. 2010) sinking towards the centre of the clusters' potential wells. The physical conditions giving rise to cooling flows depend on the properties of the ICM and the hosting cluster. In particular, if the central ($r \lesssim$ 10–100 kpc, $\sim$10 per cent of the virial radius; e.g. White, Jones & Forman 1997; Hudson et al. 2010; McDonald et al. 2017) density of the ICM in dynamically relaxed clusters is 0.1 cm^{-3} and its temperature (as obtained from X-ray observations) is $\sim 10^7$ K, the ICM ought to cool via thermal bremmstrahlung on a time-scale significantly shorter than the Hubble time (e.g. Peres et al. 1998; Voigt & Fabian 2004). These cosmologically rapidly cooling regions are referred as 'cool cores' and today are believed to characterize roughly a third of all galaxy clusters (e.g. McDonald et al. 2018), the so-called cool-core clusters. According to their properties, cooling flows could drive to the BCG region star-forming gas at huge rates. As a matter of fact, if the total mass of the ICM in cool cores is integrated and divided by the cooling time, the theoretical isobaric ICM cooling rate for a massive galaxy cluster (e.g. White et al. 1997; Peres et al. 1998; Allen et al. 2001; Hudson et al. 2010) would be of the order of $\sim 10^2$–10^3 M$_\odot$ yr^{-1}, thus implying a massive stream of gas falling on to the central BCG (of the order of 10^{11}–10^{12} M$_\odot$ within the cluster dynamical time). None the less, the search for this cold ICM found far less cold gas and young stars than predicted (e.g. Johnstone, Fabian & Nulsen 1987; Hatch et al. 2005; Hoffer et al. 2012; Molendi et al. 2016). Specifically, these works showed that local cool-core clusters lack signatures of the massive cooling flows predicted by classical models since their central galaxies form new stars at $\sim$1 per cent of the predicted rate. This fact became known as the *cooling flow problem*. A first answer to the problem came with the advent of the *Chandra Observatory* high-resolution X-ray imaging showing that the ICM in cool-core clusters was not at all relaxed as supposed, but highly dynamic, due to the effects of BCG-hosted radio-loud AGNs (e.g. Sun 2009). Indeed, the AGNs' strong interaction with the ICM can be at the origin of large bubbles in the gas, possibly inflated by the radio jets (e.g. Bîrzan et al. 2004; Forman et al. 2007; Hlavacek-Larrondo et al. 2015) and rising in size buoyantly, as well as outflows, cocoon shocks, sonic ripples, and turbulent mixing (e.g. Gaspari, Ruszkowski & Oh 2013). The amount of mechanical energy released by AGNs is thought to counterbalance the ICM radiative losses due to the cooling effectively (e.g. McNamara & Nulsen 2007; Fabian 2012; McNamara & Nulsen 2012), thus suggesting that 'mechanical feedback', heating the ICM, could prevent the massive inflows of gas predicted by classical models with BCGs accreting inefficiently via 'maintenance mode' (e.g. Saxton et al. 2005; also referred to as 'low-excitation' or 'radio mode'). Spatially resolved X-ray spectroscopic observations carried on with *XMM–Newton* and *Chandra* in the early 2000s (e.g. Kaastra et al. 2001; Pettini et al. 2001; Peterson et al. 2003; Peterson & Fabian 2006) revealed that the bulk of the ICM cooling was being quenched at temperatures above one-third of its virial value ($\sim$1 keV). These spectroscopic observations, corroborating findings from the *FUSE* satellite and the Cosmic Origins Spectrograph on the *Hubble Space Telescope* (*HST*), set upper limits on the amount of cooling material below $\sim 10^7$ K, lowering previous estimates by an order of magnitude ($\sim$10 per cent), i.e. $\sim$30 M$_\odot$ yr^{-1} (e.g. Salomé & Combes 2003; Bregman et al. 2005; McDonald et al. 2014; Donahue et al. 2017).

As a consequence of all these findings, nowadays cooling flows are not believed anymore to explain the stellar mass growth of BCGs but their ongoing star formation and AGN activity through thermally unstable cooling of the ICM into warm and cold clouds sinking towards the BCG (e.g. *chaotic cold accretion*; Gaspari & Sądowski 2017; Tremblay et al. 2018). Still elusive, the BCG formation scenario seems to be driven by galactic cannibalism, i.e. the merging of the BCGs' progenitors with satellite galaxies that gradually sink towards the cluster centre due to dynamical friction. The time-scale of this process is inversely proportional to the satellite mass, hence promoting preferential accretion of massive cluster companions. Recent simulations seem to point out that after an initial monolithic build-up of the BCGs' progenitors and the virialization of the hosting halo, the mass growth of BCGs at $z \lesssim 1$ is dominated by galactic cannibalism, and specifically through *dry* (or dissipationless) mergers, i.e. gas poor and involving negligible star formation (e.g. Khochfar & Burkert 2003; De Lucia & Blaizot

Downloaded from https://academic.oup.com/mnras/article/487/4/5593/5514359 by guest on 26 November 2020

2007; Vulcani et al. 2016). In this scenario for the hierarchical formation of galaxies, star formation at $z \lesssim 1$ should contribute only marginally to the BCG stellar mass as confirmed from studies on BCGs at low redshift (i.e. $z < 0.3$; e.g. Pipino et al. 2009; Donahue et al. 2010; Liu, Mao & Meng 2012; Fraser-McKelvie, Brown & Pimbblet 2014).

In this framework, we study the BCG inhabiting the cool-core cluster Abell 2667, a richness class-3 cluster in the Abell catalogue (Abell 1958), located in the Southern celestial hemisphere [i.e. RA(J2000.0) = $23^{h}51^{m}39\overset{s}{.}37$; Dec(J2000.0) = $-26^{\circ}05'02\overset{''}{.}7$), at redshift $z = 0.2343$. Abell 2667 is known for its gravitational lensing properties, due to the presence of several multiple-image systems and a bright giant arc in its core (e.g. Rizza et al. 1998; Covone et al. 2006). Because of its extremely high X-ray brightness (i.e. $L_X = (14.90 \pm 0.56) \times 10^{44}\, h_{70}^{-2}$ erg s^{-1} within the 0.1–2.4 keV band; Rizza et al. 1998), Abell 2667 is one of the most luminous X-ray galaxy clusters in the Universe. According to the cluster's regular X-ray morphology (Rizza et al. 1998) and the dynamics of its galaxies (Covone et al. 2006), Abell 2667 has been classified as a dynamically relaxed cluster showing the additional characteristic of a drop in the ICM temperature profile within its central region. Therefore, the cluster hosts a cool core with an estimated cooling time of $t_{cool} = 0.5$ Gyr, as derived from *Chandra* data by Cavagnolo et al. (2009). Using the National Radio Astronomy Observatory (NRAO) VLA Sky Survey radio data at 1.4 GHz, Kale et al. (2015) listed the Abell 2667 central galaxy as a radio-loud source with a radio power of $P = 3.16 \times 10^{24}$ W Hz^{-1}, thus corroborating the AGN classification of the galaxy by Russell et al. (2013). The analysis of *Chandra* data has confirmed the presence of an AGN in a recent work by Yang et al. (2018). Specifically, the authors classify the BCG as a type 2 AGN (i.e. an AGN with its broad-line region, BLR, obscured) with an unabsorbed rest-frame 2–10 keV luminosity of $2.82^{+5.50}_{-1.70} \times 10^{43}$ erg s^{-1}. In addition to AGN activity, in Rawle et al. (2012), the authors reported the BCG is forming stars at a rate, inferred from the far-IR via the spectral energy distribution (SED) templates by Rieke et al. (2009), equal to $8.7 \pm 0.2\, M_{\odot}$ yr^{-1}. Ultimately, the presence of narrow (full width at half-maximum, FWHM < 1000 km s^{-1} in the source rest frame; Caccianiga et al. 2000) but strong hydrogen and nebular emission lines ([O II] λ3727, Hβ, [O III] $\lambda\lambda$4959, 5007, Hα) has been detected around the central galaxy.

Thanks to the last-generation integral field unit spectrographs such as the Multi Unit Spectroscopic Explorer (MUSE), a new and wider window on the description of the physical processes characterizing galaxies beyond the Local Universe has been opened. Our work aims at exploiting the exquisite quality of these new data in order to investigate in more detail the nature of the Abell 2667 central galaxy, spatially resolving the phenomena that the galaxy is undergoing.

This paper is structured as follows. After the description in Section 2 of the data sets used in this work, we present our methods and results in Section 3. Specifically, in Section 3.1 we describe the BCG structural properties as retrieved from the analysis of *Hubble Space Telescope* multiwavelength imaging data while in Sections 3.2 and 3.3 we report the results from the MUSE analysis of the BCG stellar and gas components, respectively. Ultimately, in Section 4, we summarize our findings and report different plausible scenarios describing the observed phenomena taking place within the Abell 2667 BCG.

Throughout this paper, we adopt a flat lambda cold dark matter (ΛCDM) cosmology of $\Omega_M = 0.307$, $\Omega_\Lambda = 0.693$, $H_0 = 67.7$ km s^{-1} Mpc^{-1}. According to this cosmology, the age of the Universe at $z = 0.2343$ is 10.92 Gyr, while the angular scale is 3.844 kpc arcsec^{-1}. If not differently stated, the star formation rates and stellar masses reported in this paper are based on a Chabrier (2003) initial mass function (IMF), while the magnitudes are in the AB system.

2 DATA

Abell 2667 was observed with the integral field spectrograph MUSE (Bacon et al. 2014) at the Very Large Telescope (UT4-Yepun) under the GTO programme 094.A-0115(A) (P. I. J. Richard) on 2014 October 26. The MUSE pointing is composed of four exposures of 1800 s, each one centred on the BCG but with slightly different field-of-view (FoV) rotations to mitigate systematic artefacts. The raw data are publicly available on the ESO Science Archive Facility[1] and we reduce them through the standard calibrations provided by the `eso-muse pipeline` (Weilbacher et al. 2014), version 1.2.1. The final data cube has a field of view of 1 arcmin^2 (corresponding to $\sim$230 $\times$ 230 kpc), with a spatial sampling of 0.2 arcsec in the wavelength range 4750–9350 Å. Throughout the observations, the source was at an average airmass of 1 with an average *V*-band (DIMM station) observed seeing of $\sim$0.96 arcsec (FWHM). To reduce the sky residuals, we apply the Zurich atmosphere purge (ZAP version 1.0; Soto et al. 2016) using a SExtractor (Bertin & Arnouts 1996) segmentation map to define sky regions.

In our work, in addition to MUSE, we make use of ancillary data from the *Hubble Space Telescope*. The publicly available and fully reduced (Hubble Legacy Archive[2]) *HST* observations of the Abell 2667 cluster were taken on 2001 October 9–10 under the GO programme 8882 (Cycle 9; P.I. S. Allen). The observations, covering a mosaic FoV wider than 1.8 arcmin $\times$ 1.8arcmin, were carried out with the WFPC2 in the *HST* filters (WF3 aperture): F450W (5 $\times$ 2400 s), F606W (4 $\times$ 1000 s), F814W (4 $\times$ 1000 s).

3 ANALYSIS AND RESULTS

In the following section, we describe the analysis of both the *HST* and MUSE data sets which allows us to probe the BCG structural properties (e.g. total magnitude, Sérsic index, effective semimajor axis, axis ratio, position angle), as well as its stellar and gas components. The structural parameters are obtained thanks to GALFITM (Häußler et al. 2013; Vika et al. 2013) on *HST* data. From MUSE data we obtain results on the galaxy stellar component thanks to pPXF (i.e. penalised PiXel-Fitting; Cappellari & Emsellem 2004) and SINOPSIS (i.e. SImulatiNg OPtical Spectra wIth Stellar population models; Fritz et al. 2007), which allow for a study of the spatially resolved stellar kinematics and the galaxy star formation rate (SFR), respectively. Finally, the gas is studied employing tailored scripts. Most of the results are achieved coding in PYTHON and partially implementing the MUSE PYTHON data analysis framework (MPDAF; Bacon et al. 2016, Conseil et al. 2016, Piqueras et al. 2017).

3.1 Structural properties

The surface brightness profile of the BCG is fitted with a Sérsic (1968) function in the F450W, F606W, and F814W *HST* WFPC2 filters. To this aim, we use GALFITM, a multiwavelength version of

[1] http://archive.eso.org/cms.html
[2] https://hla.stsci.edu/

Downloaded from https://academic.oup.com/mnras/article/487/4/5593/5514359 by guest on 26 November 2020

GALFIT (Peng et al. 2010) that enables the simultaneous measurement of surface brightness profile parameters in different filters. The code allows the user to set the variation of each parameter (centroid coordinates, total magnitude $m_{\rm tot}$, Sérsic index n, effective semimajor axis $R_{\rm e}$, axis ratio b/a, and position angle PA) as a function of wavelength, through a series of Chebyshev polynomials with a user-specified degree (cf. Vika et al. 2013, for further details). We adopt a bright unsaturated and isolated field star as the point spread function (PSF) image.

One of the main problems to address when fitting the surface brightness profile of BCGs consists in accurately subtracting the sky background, as well as the intracluster light (ICL) in the crowded central regions of the clusters. In particular the ICL, if not considered, tends to increase both the size and the total luminosity of the BCG (Bernardi et al. 2007). Hence, although estimating the light profile of the ICL is beyond the scope of this work, we took it into account by fitting the bright galaxies in the field, and the BCG + ICL, in separate steps, following an approach similar to that used in Annunziatella et al. (2016), as summarized below. First, we fitted together the BCG with all the (20) bright sources included in a field of view of 60 arcsec × 60arcsec with single Sérsic profiles, while masking the faintest objects, and the gravitational arcs present in the field. In this first fit we left both the sky and the BCG Sérsic parameters free as a function of wavelength, while forcing all the parameters (but the magnitudes) of the surrounding galaxies to remain constant in the three filters, to reduce the computational time (with Chebishev polynomial degrees set to 1 and 3, for the BCG and the other objects, respectively; Häußler et al. 2013). In each filter, we derived the residual map of the BCG + ICL + sky by subtracting the best-fitting models of the surrounding galaxies from the original image. Then, we used this image, opportunely masked in the regions with strong residuals, to fit the BCG and the ICL separately. We fitted single Sérsic functions to both components, constraining the Sérsic index of the ICL within the range 0.2–1, since its surface brightness profile is known to have a flat core and sharply truncated wings (e.g. Annunziatella et al. 2016; Merlin et al. 2016). In order to better estimate the sky background and the parameter uncertainties, we performed a series of GALFITM runs with different initial settings, by varying the Chebishev polynomial degrees. We start (i) by forcing all the BCG and ICL parameters (but the magnitudes) to be constant as a function of wavelength in the fit. Then, in the following runs, we increasingly relax the degrees of freedom of the system, by leaving as free parameters: (ii) $m_{\rm tot}$ and $R_{\rm e}$; (iii) $m_{\rm tot}$, $R_{\rm e}$, n; and (iv) all the parameters. This is done for both the BCG and the ICL, in all the allowed combinations, for a total of 16 different runs. As expected, the best reduced χ^2 is obtained for the fit with the largest number of degrees of freedom (all parameters free for both the BCG and ICL profiles).[3] However, we derive our estimates for the structural parameters of the BCG as the average among the results of all the GALFITM runs in each filter, as shown in Table 1. In this table, instead of the formal GALFITM uncertainties (based on the χ^2 test), which are unrealistically small, we report the variation range for each parameter. Mean values averaged out among the three different filters are also shown.

From the results, we note that the derived circularized half-light radius of the BCG is in good agreement with the values reported in the literature (e.g. Newman et al. 2013a,b) while the highly centrally peaked Sérsic profile (n = 4.5–5.0) suggests that the galaxy is a massive dispersion-dominated spheroid.

The two-dimensional models of the galaxy light profile in each *HST* filter are then subtracted from the original observations, thus allowing for a visual estimate of the quality of the fit and, simultaneously, the detection of possible (sub-)structures not reproduced by the single Sérsic profile. In Fig. 1, we present the zoomed-in cutouts (∼16 arcsec × 16 arcsec) of the F450W, F606W, and F814W *HST* images before (upper panels) and after (bottom panels) the subtraction of the GALFITM model (middle panels). In the top panel, there is clear evidence of clumpy structures together with a more diffuse emission extending along the spatial projected direction of the galaxy major axis, and in particular at the north-east and south-west extremities of the BCG. The subtraction of the models from data highlights these clumps, showing they reside in filaments extending from the galaxy outskirts down to its very centre. Even though these substructures can be detected in all *HST* bands, the most intense and structured emission comes from the bluer filter, i.e. F450W. This fact suggests that the light coming from the filaments is principally originated from young stellar populations.

3.2 Stellar component

In order to spatially resolve the properties of the BCG stellar component (stellar kinematics, mass-building history) we resort to pPXF(Cappellari & Emsellem 2004) and SINOPSIS (Fritz et al. 2007). In the following subsections, we describe the results obtained from the two different codes, dividing the pPXF output (see Section 3.2.1) from SINOPSIS findings (see Section 3.2.2).

3.2.1 Stellar kinematics

To spatially resolve the BCG stellar kinematics we probe each spaxel (i.e. spatial pixels) of the MUSE data cube where the signal-to-noise ratio (SNR) of the stellar continuum is >3. Specifically, we compute the SNR as the median value of the ratio between the observed flux and error in each channel of the data cube corresponding to the 5250–6250 Å rest-frame wavelength range. We adopt this interval of wavelengths since old stellar populations dominate its flux and there are no strong emission lines. Whenever SNR < 3, we perform a fifth-order polynomial fit to the observed spectra in order to remove any deviation from linearity due to noise or bad sky reduction, whereas if SNR > 3, we proceed with a pPXF fit implementing the UV-extended ELODIE models by Maraston & Strömbäck (2011). These models are based on the stellar library ELODIE (Prugniel et al. 2007) merged with the theoretical spectral library UVBLUE (Rodríguez-Merino et al. 2005). The single stellar population models (SSPs) that constitute the UV-extended ELODIE models have a Salpeter IMF (Salpeter 1955), a solar metallicity ($Z = 0.02$), a resolution of 0.55 Å (FWHM), and a spectral sampling of 0.2 Å, covering the wavelength range 1000–6800 Å. The models span 54 ages, ranging from 3 Myr to 15 Gyr. To optimize the pPXF absorption line fits, we mask the region about the most prominent emission lines (see Table 2) in the BCG spectra, along with the telluric lines at 5577, 5889, 6157, 6300, and 6363 Å, whose residuals could potentially contaminate the spectra. We resolve to sixth-order additive polynomials and first-order multiplicative polynomials corrections for the continuum.

In Fig. 2, the maps of the stars' line-of-sight velocity ($\Delta v_\star$) and velocity dispersion ($\sigma_\star$) are presented. The stars' line-of-sight velocities are relative to the BCG systemic velocity (i.e. $v_{\rm sys} \simeq$

[3]In Fig. A1 (appendix) we present the BCG surface brightness profile and its best fit for the F814W filter.

Downloaded from https://academic.oup.com/mnras/article/487/4/5593/5514359 by guest on 26 November 2020

Table 1. List of the GALFITM output parameters (and their variation range) for the Abell 2667 BCG.

Band	$m_{\rm tot}$ (mag)	$\Delta m_{\rm tot}$ (mag)	n	Δn	$R_{\rm e}$ (arcsec)	$\Delta R_{\rm e}$ (arcsec)	$R_{\rm e,circ}$ (arcsec)	b/a	$\Delta b/a$	PA (deg)	ΔPA (deg)
F814W	16.31	16.21 – 16.50	4.97	4.44 – 5.52	9.28	6.83 – 11.01	8.15	0.77	0.76 – 0.80	50.10	49.56 – 51.39
F606W	17.14	17.01 – 17.32	4.40	3.86 – 4.72	8.69	6.81 – 10.42	7.52	0.75	0.73 – 0.77	49.80	49.56 – 50.29
F450W	18.30	18.18 – 18.39	4.55	4.33 – 4.72	7.84	6.72 – 9.19	6.79	0.75	0.71 – 0.77	46.78	37.84 – 49.86
Mean	–	–	4.64	4.21 – 5.00	8.60	6.78 – 10.21	7.49	0.76	0.73 – 0.78	48.89	45.09 – 50.51

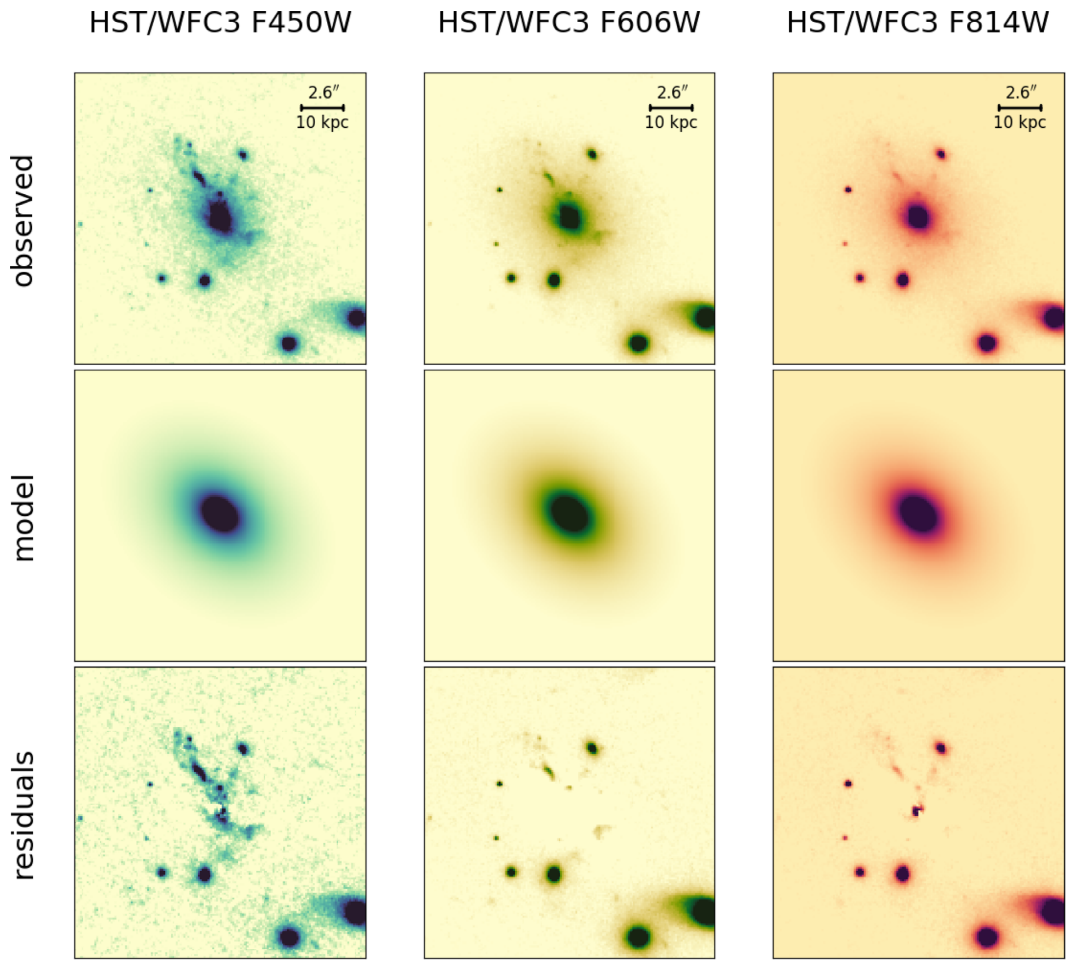


Figure 1. *HST* images of the innermost region of Abell 2667 in the optical filters F450W, F606W, and F814W (from left to right). From top to bottom, we present the original reduced *HST* observations (P. I. S. Allen, https://hla.stsci.edu/), the two-dimensional GALFITM models of the BCG surface brightness profile, and, ultimately, the map of the residuals, obtained subtracting from the original *HST* images the GALFITM models.

$1.36 \times 10^5\,{\rm km\,s^{-1}}$) while the values of the velocity dispersion are corrected for instrumental broadening. Although both maps show no evidence of a coherent kinematic pattern (e.g. rotation), stars along the same projected direction as the *HST* blue filaments (see Section 3.1) appear to all be redshifted. This fact is indicative of their common spatial displacement, or motion, with respect to the BCG main stellar component.

Our findings on the stellar kinematics suggest that the BCG is a dispersion-supported system (as already pointed out by the value of the Sérsic index in Section 3.1) because of the stars' low maximum velocity difference ($\Delta v_\star < 150\,{\rm km\,s^{-1}}$) and high central dispersion ($\sigma_0 \sim 216 \pm 21\,{\rm km\,s^{-1}}$). The central dispersion of the galaxy is calculated averaging all the dispersion values in the right-hand panel of Fig. 2 within a circular aperture of 0.96 arcsec (i.e. the seeing FWHM) centred at the galaxy coordinates.

The BCG central velocity dispersion allows us to obtain a rough estimate of the mass of the galaxy supermassive black hole (SMBH) thanks to the $M_{\rm SMBH}$–σ_0 relation by Zubovas & King (2012):

$$M_{\rm SMBH} \sim 28 \times 10^8\,\sigma_{200}^4\,[{\rm M}_\odot], \quad (1)$$

where σ_{200} is the stellar velocity dispersion in units of $200\,{\rm km\,s^{-1}}$. According to the relation above, valid for elliptical galaxies in a cluster, the BCG SMBH mass is equal to $3.8^{+1.7}_{-1.3} \times 10^9\,{\rm M}_\odot$, with the uncertainties obtained propagating the errors on σ_0. In agreement with fig. 3 in Smolčić (2009), high values for the SMBH mass are typical of low-excitation galaxies such as LINERs, while

Downloaded from https://academic.oup.com/mnras/article/487/4/5593/5514359 by guest on 26 November 2020

Table 2. List of the most prominent emission lines (em. l.) detected in the Abell 2667 BCG spectra. The value of the rest-frame wavelength of each line (column 2) was taken from the NIST Atomic Spectra Database (https://www.nist.gov/pml/atomic-spectra-database). Finally, the third column reports whether the line is single (s) or a doublet (db).

em.l.	$\lambda_{\rm vacuum}$ (Å)	e.m.l. type
[Ne III]	3868.760	s
He I	3888.648	s
H8	3889.064	s
[Ne III]	3967.470	s
H7	3970.075	s
[S II]	4068.600	s
H ϵ	4076.349	s
H δ	4101.760	s
H γ	4340.472	s
H β	4861.333	s
[O III]	4958.911/5006.843	db
[N I]	5200.257	s
[O I]	6300.304/6363.776	db
[N II]	6548.050/6583.450	db
H α	6562.819	s
[S II]	6716.440/6730.810	db

they are statistically seldom found in high-excitation galaxies (e.g. Seyferts).

3.2.2 *Stellar population*

To derive the properties of the stellar populations of the BCG, we use SINOPSIS (Fritz et al. 2007). SINOPSIS is a code that allows the user to derive spatially resolved stellar mass and star formation rate maps of galaxies at different cosmological epochs, through the combination of theoretical spectra of SSPs. We refer the reader to Fritz et al. (2017) for a complete description of the code and on further details on the adopted models.

For each spaxel of the data cube, SINOPSIS measures the galaxy stellar mass ($M_\star$), taking into account both stars that are in the nuclear-burning phase and remnants (i.e. white dwarfs, neutron stars, and stellar black holes). Summing the value of all the spaxels within an elliptical region centred at the galaxy coordinates, with semimajor axis $a = 3.5$ arcsec ($\approx$13.5 kpc), axis ratio $b/a = 0.76$, and PA $= 48.89^\circ$ (for the parameters, see Table 1), the estimated stellar mass content is $M_\star \sim 1.38 \times 10^{11}\,{\rm M}_\odot$.

The BCG building history is reconstructed through the composition of the multiple SSPs. Although SINOPSIS obtains the best fit of spectra using up to 11 SSPs of different ages,[4] the relatively high temporal resolution provided by these SSPs does not allow us to recover the star formation history (SFH) as a function of stellar age, because of an intrinsic degeneracy in the typical features of spectra of similar age and different dust attenuation (for further details, see Fritz et al. 2007). To overcome this degeneracy, the 11 age bins are then rearranged into four epochs that display the main stages of the galaxy building history. The four epochs are carefully chosen to maximize the differences in the spectral features of the different stellar populations. For each one of the four age intervals, we present the BCG maps of the SFR in Fig. 3 and the spatially integrated SFR and percentage of mass built in Fig. 4 (*top panels*). While the SFR for look-back time > 0.02 Gyr is obtained from the best-fitting relative weights of the different SSPs reproducing the spectra continuum, the SFR at epochs ≤ 0.02 Gyr (i.e. the current SFR) is instead retrieved from the emission lines (see Fritz et al. 2017). Even though different mechanisms can be at the origin of the emission lines (e.g. star formation, AGN activity), SINOPSIS does not distinguish between these different processes and interprets the total flux of the emission lines as originated only from star formation. Because our source is known to host an X-ray-obscured AGN, the values of the current SFR have to be considered upper limits. For this reason in Section 3.3.2, as a consequence of a more accurate fit of the emission lines in the spectra, we resort to spectroscopic diagnostic diagrams (e.g. Baldwin, Phillips & Terlevich 1981) to determine the predominant mechanism originating the lines in each spaxel of the MUSE data cube. None the less, according to the maps of Fig. 3, the bulk of the BCG (i.e. $57.2^{+11.6}_{-11.7}$ per cent of the total galaxy stellar mass) was assembled more than 5.6 Gyr ago ($z > 0.7$), while spatially limited star formation (SF) episodes seem to have taken place in the outer regions at later times, forming $39.1^{+12.2}_{-12.7}$ per cent ($0.6 < t_{\rm lb} \leq 5.6$ Gyr), $3.1^{+1.6}_{-1.9}$ per cent ($0.02 < t_{\rm lb} \leq 0.6$ Gyr), and $0.6^{+1.2}_{-0.5}$ per cent ($t_{\rm lb} \leq 0.02$ Gyr) of the BCG $M_\star$, respectively. These secondary bursts of SF have highly irregular shapes that could be interpreted as the result of accretion of gas from an external source, e.g. a merger. The map of the current star formation, tracing the SF in the last 0.02 Gyr, is obtained from the emission lines. The ongoing SF is indicative of a vigorous episode of star formation (SFR $\approx$ 55 ${\rm M}_\odot\,{\rm yr}^{-1}$) spreading out across the whole BCG, extending from the innermost regions to the outskirts. The map seems to trace the isophotes of the *HST B*-band image very effectively, corroborating the hypothesis that the observed blue filamentary structure around the galaxy (see Section 3.1) could be formed of a young stellar population. In the bottom panels of Fig. 4, we present the look-back time profiles of the percentage of total stellar mass built [i.e. $m_\star(<a, \Delta z)/M_\star$, *left-hand panel*] and SFR density [i.e. SFR/$A(<a)$, *right-hand panel*] in the BCG's nuclear and outskirt regions. The left-hand panel shows that the nuclear region and the outskirts had a similar mass assembly history, suggesting that the galaxy mass assembly occurred through similar processes (e.g. major merger). The only difference between the histograms is the relative contribution to the total stellar mass (i.e. the normalization), whose trend, however, is in line with expectations: The nuclear region contributes the most to the total stellar mass. For what concerns the SFR density histogram, we see the inner regions having a more intense SFR than the outskirts. In the last 0.06 Gyr the SFR has increased significantly. In particular, in the outskirts the SFR density at $\leq$0.06 Gyr is comparable to the initial SFR density (i.e. $t_{\rm lb} \geq 5.6$ Gyr), and hence considerably higher than for $0.06 < t_{\rm lb}$ [Gyr] < 5.6. The outskirts trend is also followed by the nuclear region; however, here the current SFR appears to be a factor 5 higher. As already pointed out at the beginning of this section, this current value of the SFR density has to be considered an upper limit since it is contaminated by the AGN activity.

3.3 Gas component

The spaxel-by-spaxel subtraction of SINOPSIS synthetic stellar continua (see Section 3.2; an example of SINOPSIS fit of the BCG stellar continuum is presented in Fig. B1 of the Appendix) from MUSE observed spectra allows us to recover a pure emission line data cube. From its visual inspection, we detect a wide variety

[4]In its standard implementation, SINOPSIS uses up to 12 SSPs of different ages to reproduce the observed spectrum of a galaxy. However, according to the redshift of our target ($z = 0.2343$), the age bin corresponding to SSPs older than 11 Gyr has been excluded.

Downloaded from https://academic.oup.com/mnras/article/487/4/5593/5514359 by guest on 26 November 2020

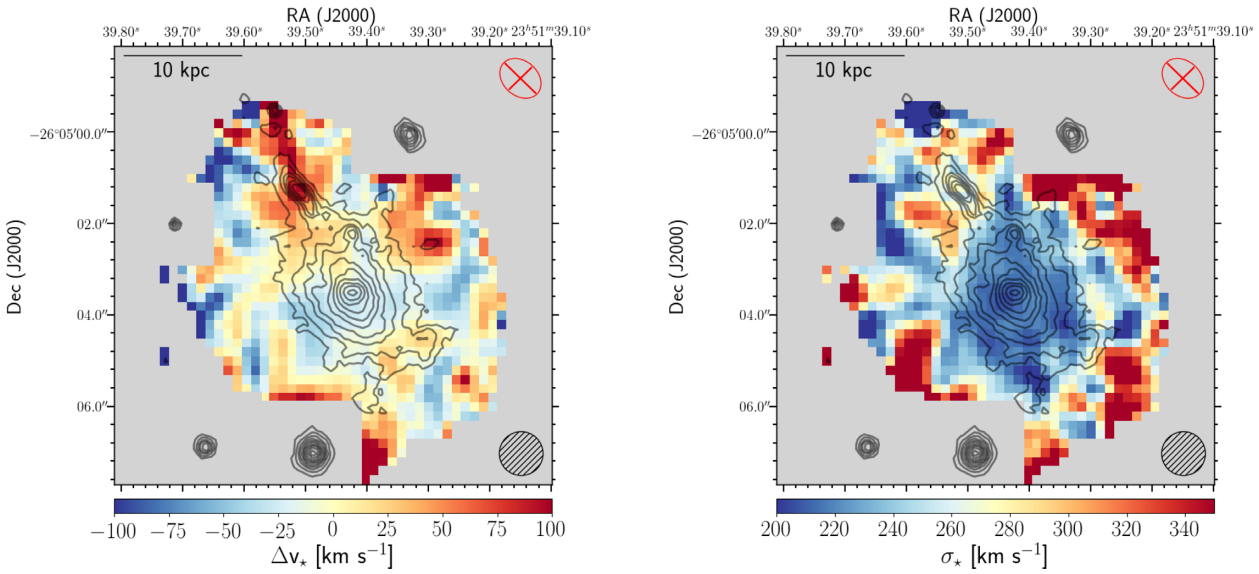


Figure 2. pPXF maps for the stellar velocity (*left-hand panel*) and velocity dispersion (*right-hand panel*) along the observer's line of sight, with the *Hubble Space Telescope* F450W WFPC2 contours superimposed (*grey solid lines*). In both maps, the spaxels with an SNR < 3 are coloured in grey. The hatched black circle on the bottom right-hand side shows the beam size of the average *V*-band observed seeing of ∼0.96 arcsec (FWHM) while the red ellipse at the top indicates the galaxy orientation in the sky-plane. The ratio between the ellipse's axes corresponds to the *b*/*a* value retrieved by the two-dimensional surface brightness model of the galaxy by GALFITM.

of line morphologies (e.g. blue wings, double-peaked lines, single lines with a broad component), a clear sign of the presence of different ongoing physical processes taking place within the BCG. Though a robust characterization of the emission line properties is not easy to recover in these conditions, we develop a PYTHON code performing for each spaxel simultaneous Gaussian line fitting for H β, [O III] λ5007, [O I] λ6300, H α, [N II] $\lambda\lambda$6548, 6583, and [S II] $\lambda\lambda$6716, 6731 (referred to as [N II] and [S II] doublets, respectively, hereafter). The code reproduces the emission lines using up to three Gaussian components. The free parameters of the code are the peak position of the Gaussians (i.e. the centroid velocity) and their standard deviation (σ) and amplitude. To reduce the significant number of total free parameters, we assumed the lines' peak position and σ of each component coupled to the others, hence assuming all the components originate from the same region of the host galaxy. While the lines' wavelength separation is fixed based on theory, the amplitudes are free to vary. The only exception is made for the [N II] doublet, whose ratio is constrained by atomic theory (e.g. Storey & Zeippen 2000).

We run the code for all the spectra with a clear detection (SNR > 3) of the H α + [N II] doublet – i.e. the strongest and most spatially extended spectroscopic feature. In Fig. 5, we present the MUSE spectra, stellar continuum, and emission line fits for five different spaxels of the BCG. These spaxels are representative of very different regions of the galaxy and its surroundings, as the morphology of the lines suggests. To estimate the errors on the parameters retrieved by our software, we perform for each spectrum 500 Monte Carlo simulations. Each Monte Carlo run is achieved perturbing the stellar-continuum-subtracted spectrum proportionally to its error, i.e. by varying the flux density according to a Gaussian distribution centred on the observed flux and with σ equal to the flux error. For each parameter, the standard deviation of the 500 Monte Carlo realizations is adopted as 1σ error. The code outputs are the flux and associated error of each emission line, thus spatially resolving the emissions. Ultimately, for each flux map, we discarded all the spaxels with an SNR lower than 3.

3.3.1 *Gas kinematics*

Due to the variety in the shape of the emission lines that characterize the spectra in our data cube, we calculate the gas line of sight velocity as the first moment of the distribution of the line fluxes. To this aim, we choose to estimate the gas velocity from the H β since it is the strongest unblended line in the spectra. In Fig. 6, the map of the gas line-of-sight velocity with respect to the BCG rest frame ($\Delta v_{\rm gas}$) is presented. The map is limited to the spaxels where the SNR of the H β is >5. The $\Delta v_{\rm gas}$ values obtained suggest that the overall gas emission is redshifted, from ∼50 km s^{-1} up to ∼200 km s^{-1}, spreading from the BCG nucleus all along the filamentary substructures revealed by *HST*. Additionally, in small areas in between the main redshifted streams of gas, the gas velocity shows a negative trend with average $\Delta v_{\rm gas} \sim -100$ km s^{-1}, thus revealing the presence of a second blueshifted gas component.

To probe in greater detail the spatial extension of the emission lines and the gas velocity, we measure the integrated flux of both H β and [O III] λ5007 in different velocity channels (e.g. McNamara et al. 2014), with respect to their rest-frame wavelength (see Table 2). The adopted bins cover the velocity ranges [−500; −100], [−100; +100], and [+100; + 500] km s^{-1}. We inquire both the H β and the [O III] λ5007 lines because of the different physical processes to which these lines are particularly sensitive, i.e. star formation and AGN activity. In Fig. 7, the integrated flux maps for H β and [O III] λ5007 are presented, highlighting in red the isocontours of the maps relative to the 85.0, 90.0, 93.0, 95.5, and 99.7 percentiles. We also show the integrated spectra of six peculiar small (1 arcsec × 1arcsec) sky regions chosen to be representative of very different areas of the galaxy, as the variety in the emission line shapes suggests. From the maps, we notice a difference in

Downloaded from https://academic.oup.com/mnras/article/487/4/5593/5514359 by guest on 26 November 2020

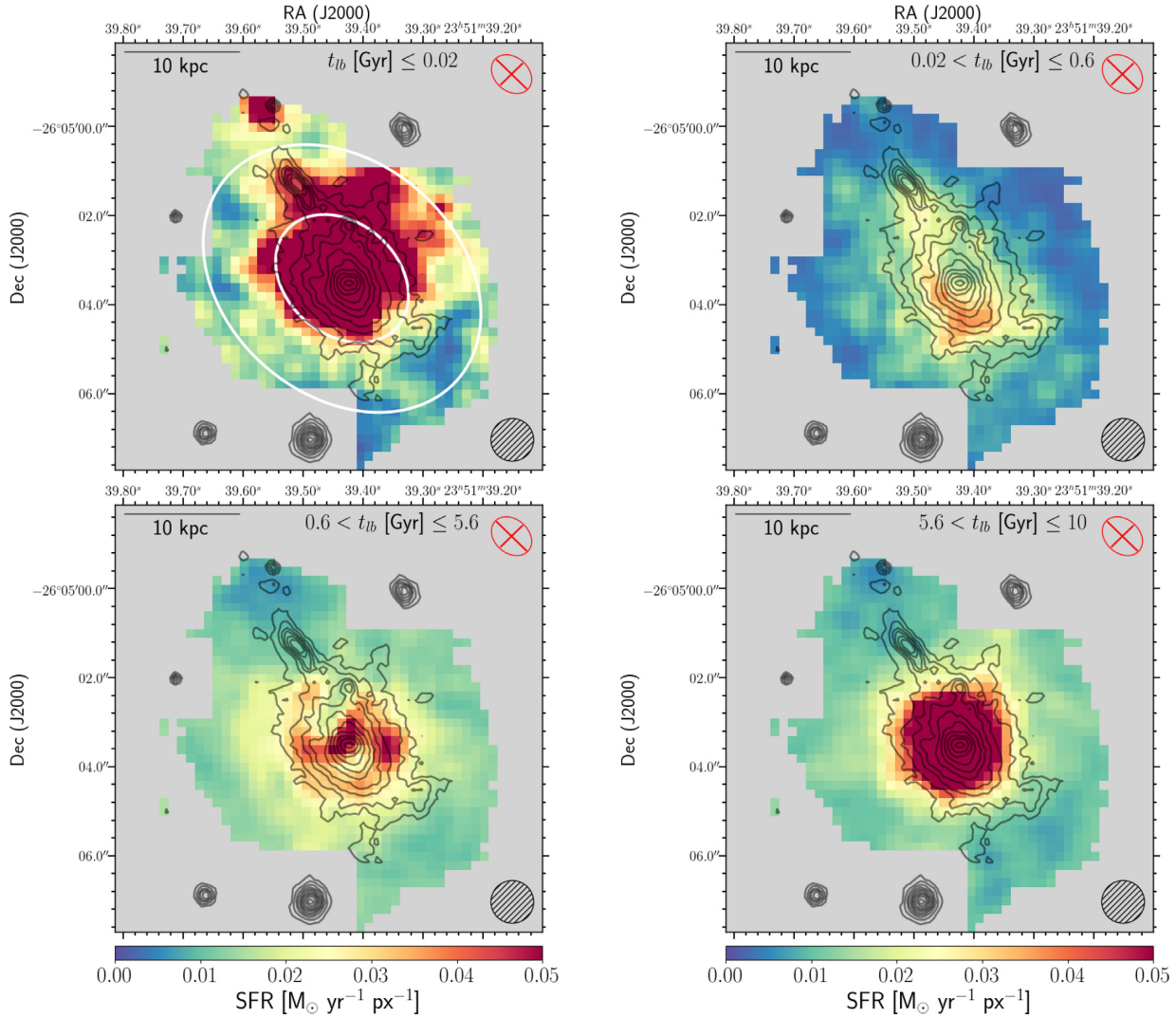


Figure 3. SINOPSIS SFR density maps of the Abell 2667 BCG in the look-back time (t_{lb}) intervals t_{lb} [Gyr] ≤ 0.02 (*top left*), 0.02 < t_{lb} [Gyr] ≤ 0.6 (*top right*), 0.6 < t_{lb} [Gyr] ≤ 5.6 (*bottom left*), and 5.6 < t_{lb} [Gyr] ≤ 10 (*bottom right*), respectively. In the top left-hand panel, the two white ellipses show the spatial extent of the regions we define as nuclear and outskirt in Fig. 4. Contours and symbols are defined as in Fig. 2.

the projected spatial extent of the two emission lines, with the H β (*top panels*) covering a wider area when compared to [O III] λ5007 (*bottom panels*), which crowds just within the BCG and some of the knots of the *HST* blue filamentary structure (see Section 3.1). However, the main result of this analysis is the detection of two gas streams: an extended and redshifted gas component (i.e. $\Delta v_{\rm gas} = [+100; +500]\,{\rm km\,s^{-1}}$) and a blueshifted one (i.e. $\Delta v_{\rm gas} = [-500; -100]\,{\rm km\,s^{-1}}$). Comparing the projected spatial extension of these two gas streams with the isophotes from the *HST* F450W image (see Fig. 7), the redshifted gas, similarly to the stars' velocity (see Section 3.2.1, Fig. 2), seems to trace the blue filamentary structure, while the blueshifted stream has a more roundish spatial extent. Similarly to recent works in the literature (e.g. Cresci et al. 2015; Venturi et al. 2018), this blueshifted gas component could be interpreted as a gas outflow originated by the activity of the central AGN.

From the maps of the [O III] λ5007, we observe at about 6 arcsec north of the BCG a weak feature (i.e. a blue spot) that has no counterparts in any of the other nebular lines in Table 2. Looking at the full integrated spectrum of the region (see Fig. C1) as well as the peculiar shape of the emission line (see spectrum F in Fig. 7, bottom panel), we interpret the blue spot as a serendipitous detection of a high-redshift line-emitting galaxy. According to the observed wavelength of the emission, the assumed galaxy would be located at $z \simeq 4.08$ if the detected line is confirmed to be Ly α.

3.3.2 *Spectroscopic diagnostic diagrams*

As already mentioned at the end of Section 3.2.2, we resort to empirical spectroscopic diagnostic diagrams, i.e. the Baldwind, Phillips and Terlevich (BPT) diagram by Baldwin et al. (1981) and the diagrams by Veilleux & Osterbrock (1987) (see also Dopita & Sutherland 1995), to discriminate the physical process originating the emission lines detected in each MUSE spectrum. This check is fundamental to retrieve a reliable value for the current BCG SFR from the map obtained by SINOPSIS (see Fig. 3, top left-hand panel). Based on the intensity ratio [O III] λ5007/H β versus [N II] λ6583/H α, [O I] λ6300/H α, and [S II] λ6716 + 6731/H α,

Downloaded from https://academic.oup.com/mnras/article/487/4/5593/5514359 by guest on 26 November 2020

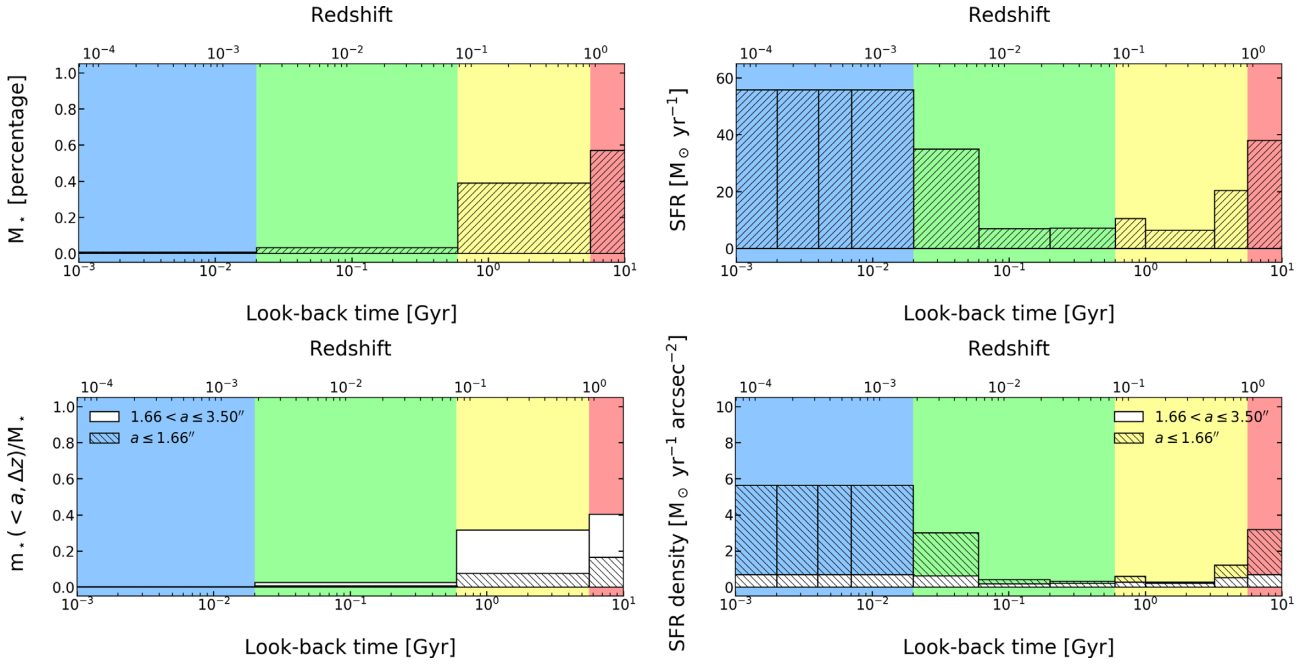


Figure 4. *Top panels*: SINOPSIS spatially integrated mass building (*left-hand panel*) and star formation history (*right-hand panel*) of the Abell 2667 BCG. The colour-shaded areas of the diagrams represent the four main age bins within which SINOPSIS calculates the galaxy percentage of mass built and the SFR (see Fig. 3). In the right-hand panel, the histogram show the SFH computed in the highest temporal resolution mode (11 SSP age intervals). Both the percentage of mass built and the SFR of each time-bin have been obtained integrating all the maps' values within an elliptical region centred at the galaxy coordinates, with axis ratio $b/a = 0.76$, position angle PA $= 48.89°$ (for the parameters see Section 3.1), and semimajor axis $a = 3.5$ arcsec. *Bottom panels*: percentage of stellar mass built (*left-hand panel*) and SFR density (*right-hand panel*) at different epochs for the nuclear (*hatched histogram*) and external regions (*white histogram*) of the BCG. For the nuclear region we have integrated SINOPSIS spatially resolved values within an elliptical aperture centred at the galaxy coordinates, with *b*/*a* and PA as before but $a = 1.66$ arcsec. For the outskirts, we have resorted to an elliptical annulus with central coordinates, *b*/*a* and PA as before, but with 1.66 arcsec $< a \leq 3.55$ arcsec. The two different areas are marked with the two white ellipses in the top left-hand panel of Fig. 3.

these empirical diagrams are commonly adopted in determining the predominant ionization mechanism giving rise to the lines. Specifically, the relative strengths of these prominent emission lines give insights into the nebular conditions of a source, thus helping separate star-forming galaxies from AGNs (LINERs and Seyferts). Thanks to the close wavelength of the lines involved, the diagrams do not suffer significantly from reddening correction or flux calibration issues. For the sake of simplicity, hereafter we will refer to these diagrams as BPT-[N II] (the original BPT diagram by Baldwin et al. 1981), BPT-[O I], and BPT-[S II] (the diagrams by Veilleux & Osterbrock 1987). To define the loci of the diagrams populated by star-forming galaxies and AGNs we resort to the empirical relations by Kewley et al. (2001). In the BPT-[N II] we adopt the equation by Kauffmann et al. (2003) to isolate the so-called transient objects (e.g. Ho 2008, and references therein).

Thanks to the multi-Gaussian fitting procedure adopted (see Section 3.3), we can deblend the H α + [N II] emission as well as the [S II] doublet. From the deblended spectra, we reconstruct spatially resolved diagnostic diagrams, being able to resolve them also in velocity channels. In particular, similarly to Mingozzi et al. (2018), we define a 'disc' and a blue- and a redshifted 'outflow' component with respect to the BCG rest-frame velocity. While the 'disc' is obtained from line fluxes within -100 to 100 km s^{-1}, the blue- and redshifted components span the -1500 to -150 km s^{-1} and 150 to 1500 km s^{-1} ranges, respectively. All the diagnostic diagrams retrieved are presented in Fig. 8 together with the empirical relations separating the different classes of objects (Kewley et al. 2001; Kauffmann et al. 2003) and the distribution of the galaxies in the Sloan Digital Sky Survey (SDSS) DR7 (Abazajian et al. 2009). The marks in the diagrams are representative of all the spaxels where the SNR of the [O III] λ5007 > 3 and they are colour-coded depending on the distance of the spaxel from the BCG centre. In each panel on the left, we additionally highlight with a black mark the position that the BCG occupies if we stack together all its MUSE spectra with SNR([O III] λ5007) > 3. The loci inhabited by the BCG in the diagrams define the galaxy unequivocally as a LINER.

If we spatially resolve the diagnostic diagrams, the line intensity ratios show that the very core of the BCG is consistent with an AGN, in agreement with Kale et al. (2015) and Yang et al. (2018), while the outer regions exhibit signs of both AGN and SF activity. We hypothesize that these two physical mechanisms could be linked to the different components of the gas we reported in Section 3.3.1. In particular, while the emission lines coming from the regions characterized by the redshifted gas stream that is cospatial with the *HST* blue filaments could trace the SF primarily, the blueshifted gas component might be related to the AGN, thus tracing a possible feedback (i.e. outflow) from the BCG active galactic nucleus (e.g. Cresci et al. 2015).

3.3.3 *Electron density*

In Fig. 9 (left-hand panel), the electron density (n_e) map of the gas is presented. The n_e values were obtained from the intensity ratio R = [S II] λ6716/[S II] λ6731 according to the empirical equation by

Downloaded from https://academic.oup.com/mnras/article/487/4/5593/5514359 by guest on 26 November 2020

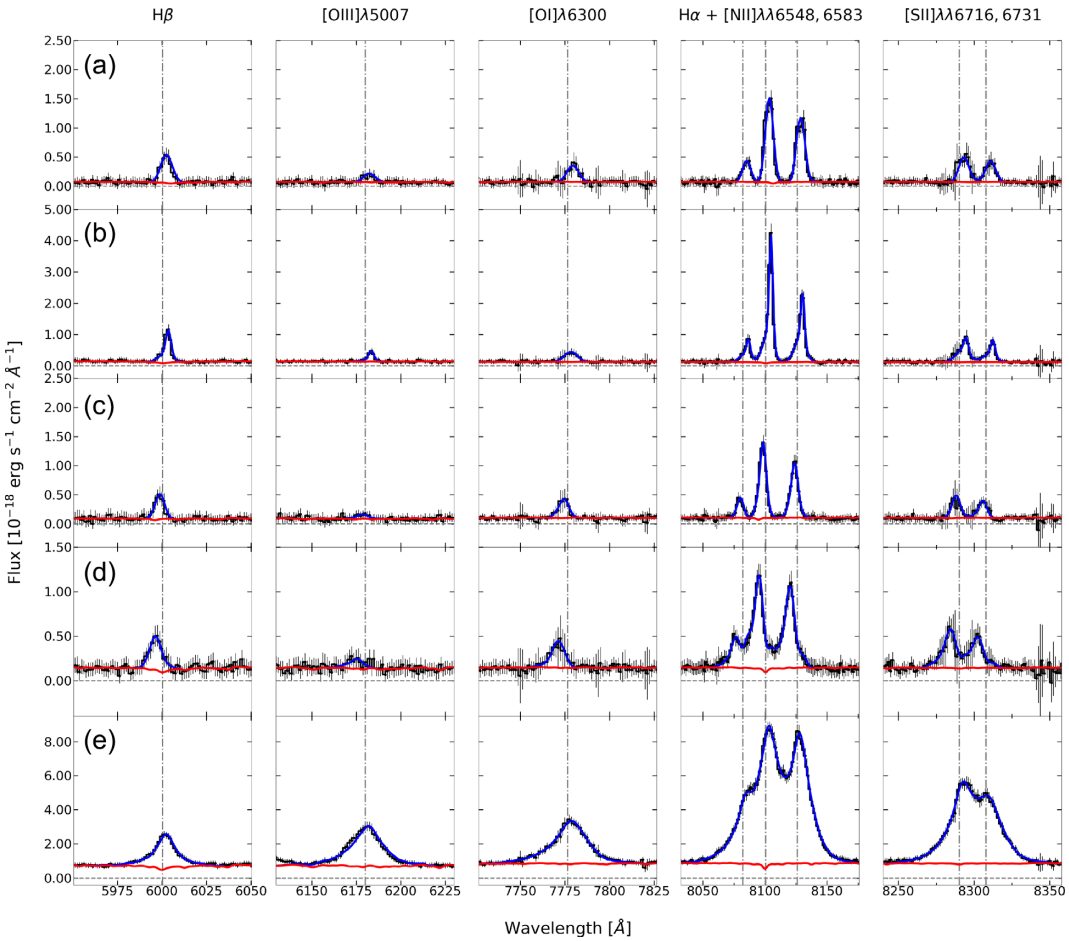


Figure 5. MUSE representative spectra and 3σ errors of the sky regions A, B, C, D, and E, presented in Section 3.3.1, Fig. 7. The *red solid line* corresponds to the SINOPSIS model of the stellar continuum while the *blue solid line* shows the fit of the spectra emission lines as obtained by our PYTHON code (see Section 3.3). The vertical dash–dotted lines are indicative of the expected wavelength of each line, according to the BCG redshift.

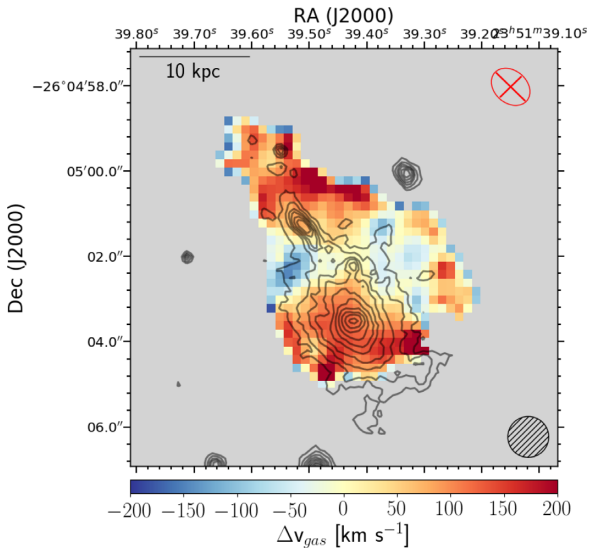


Figure 6. Map of the gas line-of-sight mean velocity ($\Delta v_{\rm gas}$) with respect to the BCG rest frame, with contours and symbols as defined in Fig. 2. The grey spaxels correspond to spectra with an SNR for the H β < 5.

Proxauf, Öttl & Kimeswenger (2014)

$$\log_{10} n_{\rm e}[{\rm cm}^{-3}] = \sim 0.0543\,\tan(-3.0553R + 2.8506) + 6.98 - 10.6905R + 9.9186R^2 - 3.5442R^3 + 0.5\,\log_{10}\left[\frac{T_{\rm e}\,[{\rm K}]}{10^4}\right] \quad (2)$$

and it was calculated supposing a spatially constant electron temperature (i.e. $T_{\rm e}$) of 10^4 K, a value widely adopted in the literature (e.g. Cresci et al. 2015) if no direct electron temperature information can be recovered from the spectra (e.g. from the diagnostic diagrams based on [O III] λλ(4958 + 5007)/λ4363 or [Ar III] λλ(7135 + 7751)/λ5192; see Proxauf et al. 2014).

A rather flat pattern for the electron density was retrieved, with a median value $n_{\rm e} \sim 10^{2.2}\,{\rm cm}^{-3}$. Only the inner region of the BCG shows a higher value for $n_{\rm e}$ although always lower than $3 \times 10^3\,{\rm cm}^{-3}$. These values are well below the critical density of the [S II] doublet, i.e. $n_{\rm e} \sim 3 \times 10^3\,{\rm cm}^{-3}$ (see Osterbrock & Ferland 2006), above which the lines become collisionally de-excited. Therefore, we can consider the electron density derived reliable within the errors. None the less, to probe a possible dependence of the electron density from the electron temperature, we let vary $T_{\rm e}$ within the range from 5000 to 26 000 K (i.e. the dashed and

Downloaded from https://academic.oup.com/mnras/article/487/4/5593/5514359 by guest on 26 November 2020

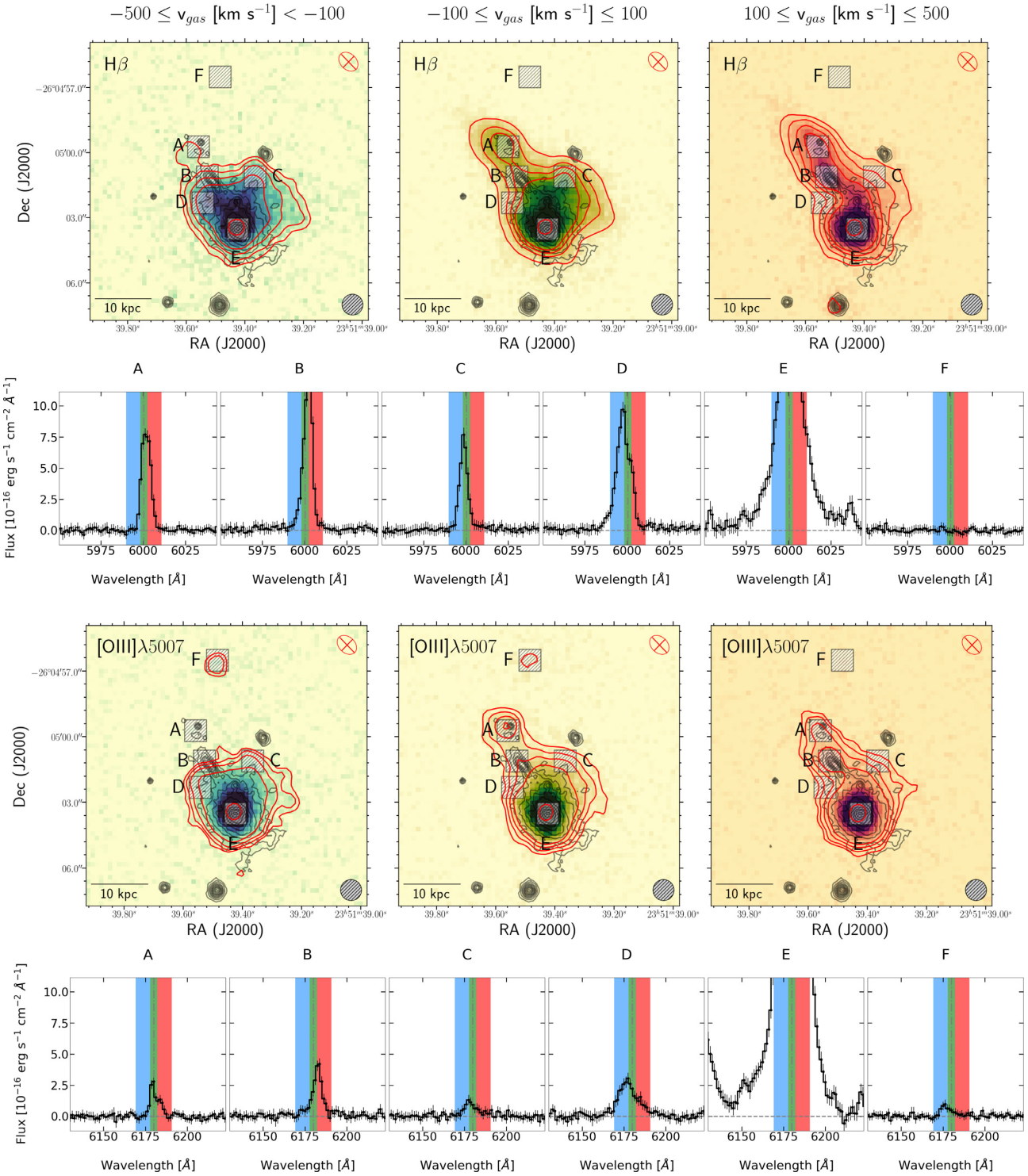


Figure 7. H β (*top panels*) and [O III] λ5007 (*bottom panels*) emission in Abell 2667 BCG with contours and symbols as defined in Fig. 2. The images show the emission line integrated flux within three different velocity channels: from -500 to -100 km s^{-1} (*blue*), from -100 to 100 km s^{-1} (*green*), and from 100 to 500 km s^{-1} (*red*). In each panel, the *red solid lines* are indicative of the 85.0, 90.0, 93.0, 95.5, and 99.7 percentiles of the emission line flux, respectively. For both H β and [O III] λ5007, we report cut-outs of the integrated spectra of six peculiar small (1 arcsec $\times$ 1 arcsec) sky regions, labelled with capital letters, and chosen to be representative of very different areas of the galaxy. In each cut-out, the shaded areas indicate the different velocity ranges we adopted.

dash–dotted lines in Fig. 9, right-hand panel, respectively). The median values for n_e do not show substantial variations, going from $\sim 10^2$ cm^{-3} (for $T_e = 5000$ K) to $\sim 10^{2.4}$ cm^{-3} (for $T_e = 26\,000$ K).

4 DISCUSSION AND CONCLUSIONS

In this paper, we have extensively analysed the properties of the BCG inhabiting the cool core cluster Abell 2667, based on both *HST* imaging and MUSE data. The bi-dimensional modelling of

Downloaded from https://academic.oup.com/mnras/article/487/4/5593/5514359 by guest on 26 November 2020

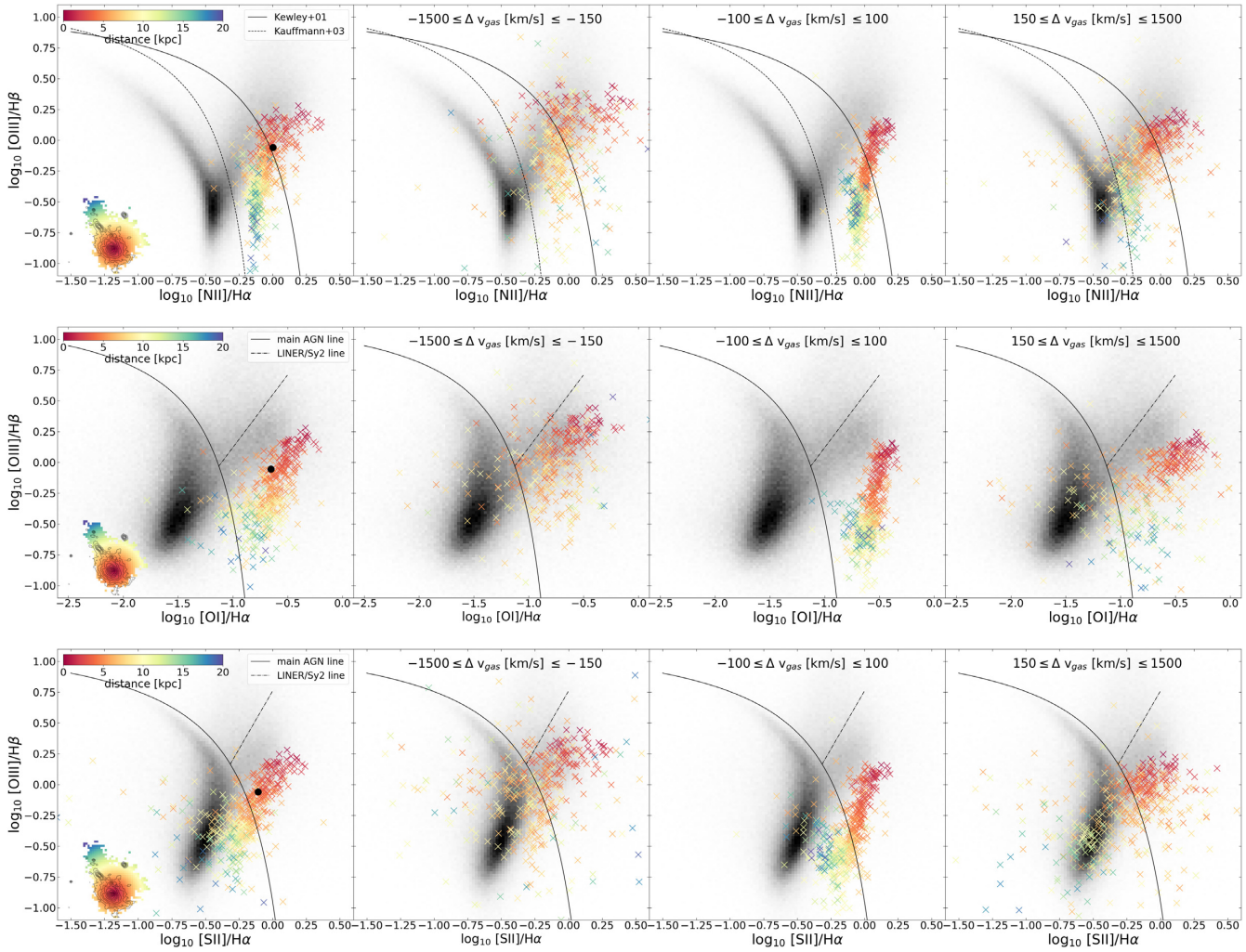


Figure 8. From top to bottom, the BPT-[N II], BPT-[O I], and the BPT-[S II] diagrams for the spaxels with SNR ([O III] λ5007) > 3. For each diagnostic, from left to right we report the diagram obtained integrating all the fluxes within −1500 km s^{-1} to 1500 km s^{-1}, and in the velocity ranges −1500 km s^{-1} to −150 km s^{-1} (*blueshifted outflow*), −100 km s^{-1} to 100 km s^{-1} (*disc*), and 150 km s^{-1} to 1500 km s^{-1} (*redshifted outflow*), respectively. Each mark is representative of a spaxel and is colour-coded according to its distance from the BCG centre (see the colourbar at the top left and the colour map at the bottom left of the left-hand panels). To separate the loci corresponding to star-forming galaxies, transition objects, and AGNs, we report the empirical relations by Kewley et al. (2001) and Kauffmann et al. (2003). Finally, we report in black the distribution of the emission line galaxies in the Sloan Digital Sky Survey DR7 (Abazajian et al. 2009).

the galaxy surface brightness profile on the *HST* images (F450W, F606W, and F814W filters) with a Sérsic law has allowed us to probe the structural properties of the BCG. The subtraction of the surface brightness model from the *HST* observations has revealed a complex system of filamentary substructures all around the BCG and lying along the projected direction of the galaxy major axis. These substructures appear to be constituted by clumps of different sizes and shapes, plunged into a more diffuse component. The *HST* intense 'blue' optical colour of these clumps is indicative of ongoing star formation activity, as also corroborated by the spatially resolved current star formation rate we obtained from MUSE spectra. Our BPT diagrams seem to further support this hypothesis since the emission arising from the clumps is 'composite', thus requiring a contribution from both the AGN and star formation. The map of the galaxy current star formation rate, i.e. the SF of the last 0.02 Gyr, shows a burst of activity with a spatially integrated rate of $\simeq 55\,M_\odot\,yr^{-1}$ extending along the same projected regions of the substructures. Our SFR is sensitively higher than the $8.7\,M_\odot\,yr^{-1}$ reported by Rawle et al. (2012) and inferred via spectral energy distribution templates (Rieke et al. 2009) from the far-infrared. However, the difference between the two estimates is merely a consequence of the methodologies applied. Both current SFRs can be considered as an upper and lower limit, respectively. In fact, while the value inferred from the far-infrared does not take into account the contribution from unobscured star formation, our estimate is contaminated by the AGN in the innermost regions of the galaxy. To solve the problem, a new spectral energy distribution analysis of the galaxy is being carried on, taking into account a multiwavelength set of data ranging from the ultraviolet to radio frequencies (Iani et al., in preparation).

According to the galaxy Sérsic index ($n = 4.64$) and its spatially resolved stellar kinematics, the BCG is a dispersion-supported spheroid with a circularized effective radius of $R_{e,circ} \simeq 30$ kpc, a low and incoherent stellar line-of-sight velocity pattern ($\Delta v_\star \leq 150\,km\,s^{-1}$) but high central velocity dispersion ($\sigma_0 \sim 216\,km\,s^{-1}$). Interestingly, the map of the stellar line-of-sight velocity reveals

Downloaded from https://academic.oup.com/mnras/article/487/4/5593/5514359 by guest on 26 November 2020

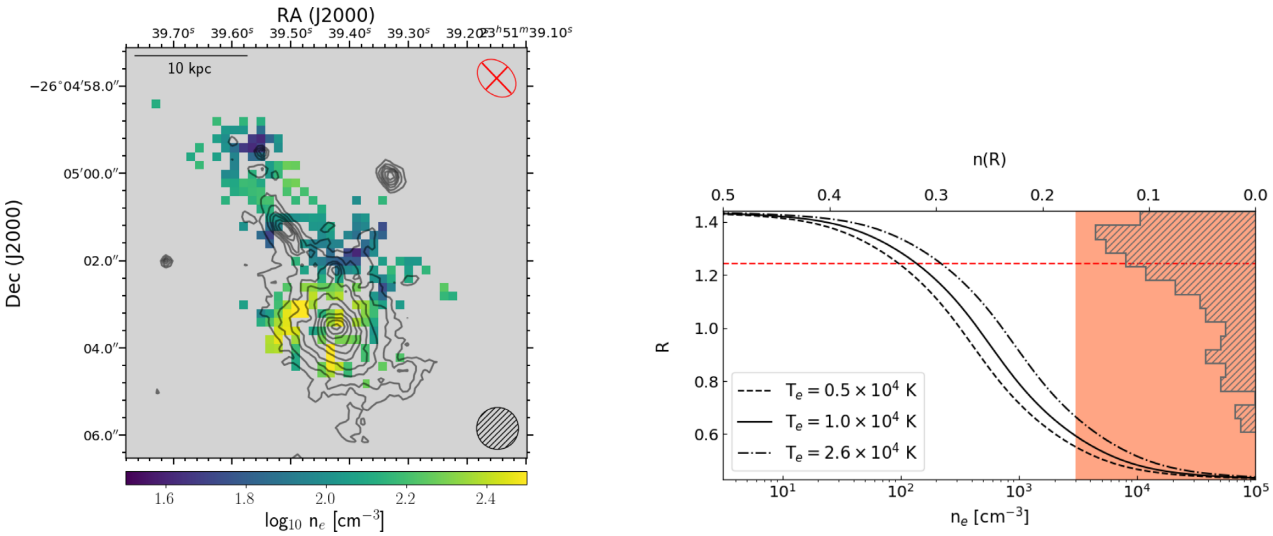


Figure 9. *Left-hand panel*: electron density (n_e) map for Abell 2667 BCG as retrieved from equation (2) for an electron temperature $T_e = 1.0 \times 10^4$ K, with contours and symbols as defined in Fig. 2. *Right-hand panel*: electron density (n_e) curve (Proxauf et al. 2014) as a function of the intensity ratio $R = $ [S II] λ6716/[S II] λ6731 for $T_e = 0.5 \times 10^4$ K (*black dashed line*), $T_e = 1.0 \times 10^4$ K (*black solid line*), and $T_e = 2.6 \times 10^4$ K (*black dash–dotted line*). The red area of the diagram highlights the electron density values above the [S II] doublet critical density (i.e. $n_e \sim 3 \times 10^3$ cm^{-3}). We present the distribution of the retrieved R values as well as the median value of the distribution $R \sim 1.21$ (*red dashed line*).

a redshifted pattern for all the spectra coinciding with the clumpy structures in the *HST* filaments, thus suggesting these stars are gravitationally bounded together and, possibly, equally distant from the BCG. The BCG radial profile of the stellar velocity dispersion suggests a positive gradient. The presence of a positive gradient has been observed in a conspicuous number of central galaxies studied with integral field unit (IFU) data (Loubser et al. 2018, Veale et al. 2018) even though its physical origin has not been understood yet. Increasing velocity dispersion profiles are usually interpreted as evidence that the diffuse stellar halo consists of accumulated debris of stars stripped from cluster members as a consequence of minor mergers ($\leq$1:4 mass ratios). However, due to the low SNR of the external spaxels in the maps of Fig. 2 and the presence of possible artefacts, our considerations on the velocity dispersion profile are limited to the most inner regions of the galaxy ($r \leq 10$ kpc).

Our estimate of the BCG stellar mass is $\sim 1.38 \times 10^{11}$ M$_\odot$. This value takes into account both stars in the nuclear-burning phase and remnants. In line with our findings on the galaxy mass assembly history, 57.2 per cent of the galaxy stellar mass was assembled more than 5.6 Gyr ago ($z > 0.7$), while in later times episodes of star formation seem to have formed the remaining 39.1 per cent ($0.6 < t_{lb} < 5.6$ Gyr), 3.1 per cent ($0.02 < t_{lb} < 0.6$ Gyr), and 0.6 per cent ($t_{lb} < 0.02$ Gyr). As shown in previous works (Kobayashi 2004; Oliva-Altamirano et al. 2015), this suggests that the BCG mass growth at high redshift ($z \geq 0.8$) has been principally driven by monolithic collapse and major mergers ($\geq$1:3 mass ratios) while at lower redshift minor mergers and cold accretion could have contributed the most to the stellar mass growth.

Our target galaxy is known to host a radio-loud type 2 AGN (Russell et al. 2013, Kale et al. 2015, Yang et al. 2018). Thus, applying the M_{SMBH}–σ_0 relation by Zubovas & King (2012), we estimate the mass of the SMBH hosted by the BCG to be equal to $3.8^{+1.7}_{-1.3} \times 10^9$ M$_\odot$. In agreement with the results obtained by Smolčić (2009) on a large survey of AGNs, the SMBH mass obtained is typical of low-excitation galaxies. This is also confirmed by our BPT diagnostic diagrams, which classify the emission coming from the BCG core as LINER. In the BCG's outskirts, the line ratios classify the observed emission as 'composite', suggesting the possible presence of both star formation and an attenuated UV radiation field from the AGN. Similar results have been obtained by Hatch, Crawford & Fabian (2007) for a sample of X-ray-bright BCGs residing in cool-core clusters at lower redshifts ($z < 0.2$), thus showing the complexity of the phenomena giving rise to line-emitting nebulæ around BCGs.

Ultimately, from the analysis of the integrated flux of the H β and [O III] λ5007 emission lines within different velocity channels, we detect the presence of two decoupled gas components with velocities in between $\Delta v_{gas} = [+100; +500]$ km s^{-1} and $\Delta v_{gas} = [-500; -100]$ km s^{-1}. The two gas components appear to cover different spatial extents, with the blueshifted stream more compact and centred around the galaxy core while the redshifted flow spreads along the regions hosting the *HST* substructures. This result shows that the gas and stars in the filaments are comoving and redshifted with respect to the observer.

To account for both the filamentary structures and the two gas components observed, two different scenarios can be invoked: a model of ICM accretion with AGN feedback and a merger. The first scenario is supported by the fact that Abell 2667 is a cool-core cluster ($t_{cool} = 0.5$ Gyr; Cavagnolo et al. 2009) and therefore, we expect the presence of an inflow of cold ICM towards the BCG. In this case, according to the *chaotic cold accretion model* (e.g. Tremblay et al. 2016; Gaspari & Sądowski 2017; Tremblay et al. 2018) and as predicted by recent theory (e.g. Pizzolato & Soker 2005; Voit et al. 2015a; Voit et al. 2015b) and simulations (e.g. Sharma et al. 2012, Gaspari et al. 2013, Li & Bryan 2014), the inflow of cold ICM would be a stochastic and clumpy event giving rise to cold giant clouds. Within these clouds, the physical conditions of the gas could satisfy the criteria for the ignition of star formation, thus explaining the observed diffuse and clumpy star-forming filaments revealed by *HST*. Since the filamentary structures extend down to the very centre of the BCG, this inflow of material could be at the origin of the galaxy AGN activity. The AGN ignition by the inflow could also be responsible for feedback through outflows that could in turn regulate the SMBH accretion in agreement with the theoretical models introduced to overcome the *cooling flow*

Downloaded from https://academic.oup.com/mnras/article/487/4/5593/5514359 by guest on 26 November 2020

problem (e.g. McNamara & Nulsen 2007; Fabian 2012; Gaspari et al. 2013). In this scenario, the redshifted stream of gas we detect would relate to the infalling material and clouds from the ICM while the blueshifted flow would be compatible with a massive ionized gas outflow originating from the SMBH. Assuming a bi-conical emission, the redshifted component of the nuclear outflow could be not revealed due to absorption from the galactic medium. An alternative flavour for this scenario, resembling what has been found in recent studies (e.g. Maiolino et al. 2017; Tremblay et al. 2018), could be taken into account too. In this case, the AGN feedback would be the mechanism triggering, influencing, and regulating the star formation within the filamentary substructures detected with *HST*. This scenario would happen if the observed substructures were made of compressed gas along possible AGN jets. Even though the physical scale at which we observe the clumps (∼10–20 kpc from the galaxy nucleus) is comparable with the above-mentioned works, we tend to exclude this hypothesis since our preliminary analysis of the public radio data set (JVLA, ALMA), as well as the X-rays (*Chandra*), of the galaxy seem to rule out the presence of jets or inflated bubbles on such a large scale.

The second scenario envisages the Abell 2667 BCG merging with a small disc-like galaxy. In this case, an infalling distorted disc of small size, coinciding with the biggest clump in the filaments, is tidally disrupted and is leaving behind streams of gas that are triggering star formation (i.e. the smaller knots) possibly because of the interaction with the BCG circumgalactic medium. Supporting this scenario, the clumps appear to lie on the BCG galactic plane, as it would happen with an accreting satellite galaxy that loses its angular momentum and starts inspiralling towards the BCG centre. At the opposite extremity of the galaxy with respect to the clumps in the *HST* images, diffuse blue emission is present, likely due to the gas left behind the satellite galaxy from a previous orbit.

We are planning a follow-up of this source in both X-rays and the radio domain since deeper observations in both electromagnetic bands will be crucial to obtain detailed information about the X-ray emission and the molecular cold gas component of this source, allowing us to disentangle the imprints of the evolutionary scenarios proposed.

ACKNOWLEDGEMENTS

We thank the anonymous referee for useful comments and a careful reading of the manuscript. This work is based on observations collected at the European Southern Observatory under ESO programmes 094.A-0115(A) and on observations made with the NASA/ESA *Hubble Space Telescope*, and obtained from the Hubble Legacy Archive, which is a collaboration between the Space Telescope Science Institute (STScI/NASA), the Space Telescope European Coordinating Facility (ST-ECF/ESA), and the Canadian Astronomy Data Centre (CADC/NRC/CSA). Giulia Rodighiero and Chiara Mancini acknowledge support from an INAF PRIN-SKA 2017 grant. Amata Mercurio acknowledges funding from the INAF PRIN-SKA 2017 programme 1.05.01.88.04. Pablo G. Pérez-Gonzalez acknowledges support from the Spanish Government grant AYA2015-63650-P. We warmly thank Stefano Ciroi and Bianca Maria Poggianti for helpful discussions.

REFERENCES

Abazajian K. N. et al., 2009, ApJS, 182, 543
Abell G. O., 1958, ApJS, 3, 211
Allen S. W., Fabian A. C., Johnstone R. M., Arnaud K. A., Nulsen P. E. J., 2001, MNRAS, 322, 589
Annunziatella M. et al., 2016, A&A, 585, A160
Auriemma C., Perola G. C., Ekers R. D., Fanti R., Lari C., Jaffe W. J., Ulrich M. H., 1977, A&A, 57, 41
Bacon R. et al., 2014, The Messenger, 157, 13
Bacon R., Piqueras L., Conseil S., Richard J., Shepherd M., 2016, Astrophysics Source Code Library, record ascl: 1611.003
Bai L. et al., 2014, ApJ, 789, 134
Baldwin J. A., Phillips M. M., Terlevich R., 1981, PASP, 93, 5
Bardelli S. et al., 2010, A&A, 511, A1
Bernardi M., 2007, AJ, 133, 1954
Bernardi M., 2009, MNRAS, 395, 1491
Bernardi M., Hyde J. B., Sheth R. K., Miller C. J., Nichol R. C., 2007, AJ, 133, 1741
Bernstein J. P., Bhavsar S. P., 2001, MNRAS, 322, 625
Bertin E., Arnouts S., 1996, A&AS, 117, 393
Best P. N., von der Linden A., Kauffmann G., Heckman T. M., Kaiser C. R., 2007, MNRAS, 379, 894
Bîrzan L., Rafferty D. A., McNamara B. R., Wise M. W., Nulsen P. E. J., 2004, ApJ, 607, 800
Bonaventura N. R. et al., 2017, MNRAS, 469, 1259
Bregman J. N., Miller E. D., Irwin J. A., 2001, ApJ, 553, L125
Bregman J. N., Miller E. D., Athey A. E., Irwin J. A., 2005, ApJ, 635, 1031
Burke D. J., Collins C. A., Mann R. G., 2000, ApJ, 532, L105
Caccianiga A., Maccacaro T., Wolter A., Della Ceca R., Gioia I. M., 2000, A&AS, 144, 247
Cappellari M., Emsellem E., 2004, PASP, 116, 138
Cavagnolo K. W., Donahue M., Voit G. M., Sun M., 2009, ApJS, 182, 12
Chabrier G., 2003, PASP, 115, 763
Conseil S., Bacon R., Piqueras L., Shepherd M., 2016, preprint (arXiv: 1612.05308)
Covone G., Kneib J.-P., Soucail G., Richard J., Jullo E., Ebeling H., 2006, A&A, 456, 409
Cowie L. L., Binney J., 1977, ApJ, 215, 723
Crawford C. S., Allen S. W., Ebeling H., Edge A. C., Fabian A. C., 1999, MNRAS, 306, 857
Cresci G. et al., 2015, A&A, 582, A63
De Lucia G., Blaizot J., 2007, MNRAS, 375, 2
Donahue M., Mack J., Voit G. M., Sparks W., Elston R., Maloney P. R., 2000, ApJ, 545, 670
Donahue M., Connor T., Voit G. M., Postman M., 2017, ApJ, 835, 216
Donahue M. et al., 2010, ApJ, 715, 881
Donahue M., de Messières G. E., O'Connell R. W., Voit G. M., Hoffer A., McNamara B. R., Nulsen P. E. J., 2011, ApJ, 732, 40
Dopita M. A., Sutherland R. S., 1995, ApJ, 455, 468
Dressler A., 1984, ARA&A, 22, 185
Dubinski J., 1998, ApJ, 502, 141
Dutson K. L., Edge A. C., Hinton J. A., Hogan M. T., Gurwell M. A., Alston W. N., 2014, MNRAS, 442, 2048
Edge A. C., Wilman R. J., Johnstone R. M., Crawford C. S., Fabian A. C., Allen S. W., 2002, MNRAS, 337, 49
Egami E., Rieke G. H., Fadda D., Hines D. C., 2006, ApJ, 652, L21
Fabian A. C., 1994, ARA&A, 32, 277
Fabian A. C., 2012, ARA&A, 50, 455
Fabian A. C., Nulsen P. E. J., 1977, MNRAS, 180, 479
Forman W. et al., 2007, ApJ, 665, 1057
Fraser-McKelvie A., Brown M. J. I., Pimbblet K. A., 2014, MNRAS, 444, L63
Fritz J. et al., 2007, A&A, 470, 137
Fritz J. et al., 2017, ApJ, 848, 132
Gaspari M., Sądowski A., 2017, ApJ, 837, 149
Gaspari M., Ruszkowski M., Oh S. P., 2013, MNRAS, 432, 3401
Hatch N. A., Crawford C. S., Fabian A. C., 2007, MNRAS, 380, 33
Hatch N. A., Crawford C. S., Fabian A. C., Johnstone R. M., 2005, MNRAS, 358, 765
Häußler B. et al., 2013, MNRAS, 430, 330
Heckman T. M., Baum S. A., van Breugel W. J. M., McCarthy P., 1989, ApJ, 338, 48

Downloaded from https://academic.oup.com/mnras/article/487/4/5593/5514359 by guest on 26 November 2020

Hlavacek-Larrondo J. et al., 2015, ApJ, 805, 35
Hoffer A. S., Donahue M., Hicks A., Barthelemy R. S., 2012, ApJS, 199, 23
Ho L. C., 2008, ARA&A, 46, 475
Hudson D. S., Mittal R., Reiprich T. H., Nulsen P. E. J., Andernach H., Sarazin C. L., 2010, A&A, 513, A37
Hu E. M., 1992, ApJ, 391, 608
Johnstone R. M., Fabian A. C., Nulsen P. E. J., 1987, MNRAS, 224, 75
Johnstone R. M., Hatch N. A., Ferland G. J., Fabian A. C., Crawford C. S., Wilman R. J., 2007, MNRAS, 382, 1246
Kaastra J. S. et al., 2001, in Giacconi R., Serio S., Stella L., eds, ASP Conf. Ser. Vol. 234, X-ray Astronomy 2000. Astron. Soc. Pac., San Francisco, p. 351
Kale R., Venturi T., Cassano R., Giacintucci S., Bardelli S., Dallacasa D., Zucca E., 2015, A&A, 581, A23
Kauffmann G. et al., 2003, MNRAS, 346, 1055
Kewley L. J., Dopita M. A., Sutherland R. S., Heisler C. A., Trevena J., 2001, ApJ, 556, 121
Khochfar S., Burkert A., 2003, ApJ, 597, L117
Kobayashi C., 2004, MNRAS, 347, 740
Lauer T. R., Tremaine S., Richstone D., Faber S. M., 2007, ApJ, 670, 249
Lauer T. R., Postman M., Strauss M. A., Graves G. J., Chisari N. E., 2014, ApJ, 797, 82
Ledlow M. J., Owen F. N., 1996, AJ, 112, 9
Lidman C. et al., 2012, MNRAS, 427, 550
Liu F. S., Mao S., Meng X. M., 2012, MNRAS, 423, 422
Li Y., Bryan G. L., 2014, ApJ, 789, 153
Loubser S. I., Hoekstra H., Babul A., O'Sullivan E., 2018, MNRAS, 477, 335
Maiolino R. et al., 2017, Nature, 544, 202
Malumuth E. M., Richstone D. O., 1984, ApJ, 276, 413
Maraston C., Strömbäck G., 2011, MNRAS, 418, 2785
Mauch T., Sadler E. M., 2007, MNRAS, 375, 931
McDonald M., 2011, ApJ, 742, L35
McDonald M., Roediger J., Veilleux S., Ehlert S., 2014, ApJ, 791, L30
McDonald M., Gaspari M., McNamara B. R., Tremblay G. R., 2018, ApJ, 858, 45
McDonald M. et al., 2017, ApJ, 843, 28
McNamara B. R., Nulsen P. E. J., 2007, ARA&A, 45, 117
McNamara B. R., Nulsen P. E. J., 2012, New J. Phys., 14, 055023
McNamara B. R. et al., 2014, ApJ, 785, 44
Merlin E. et al., 2016, A&A, 590, A30
Merritt D., 1985, ApJ, 289, 18
Mingozzi M. et al., 2018, A&A, 662, A146
Mittal R., Hudson D. S., Reiprich T. H., Clarke T., 2009, A&A, 501, 835
Molendi S., Tozzi P., Gaspari M., De Grandi S., Gastaldello F., Ghizzardi S., Rossetti M., 2016, A&A, 595, A123
Newman A. B., Treu T., Ellis R. S., Sand D. J., Nipoti C., Richard J., Jullo E., 2013a, ApJ, 765, 24
Newman A. B., Treu T., Ellis R. S., Sand D. J., 2013b, ApJ, 765, 25
O'Dea C. P., Baum S. A., Mack J., Koekemoer A. M., Laor A., 2004, ApJ, 612, 131
O'Dea K. P. et al., 2010, ApJ, 719, 1619
Oemler Jr. A., 1976, ApJ, 209, 693
Oliva-Altamirano P., Brough S., Jimmy Tran K.-V., Couch W. J., McDermid R. M., Lidman C., von der Linden A., Sharp R., 2015, MNRAS, 449, 3347
Osterbrock D. E., Ferland G. J., 2006, Astrophysics of Gaseous Nebulae and Active Galactic Nuclei. University Science Books
Ostriker J. P., Tremaine S. D., 1975, ApJ, 202, L113
Peng C. Y., Ho L. C., Impey C. D., Rix H.-W., 2010, AJ, 139, 2097
Peres C. B., Fabian A. C., Edge A. C., Allen S. W., Johnstone R. M., White D. A., 1998, MNRAS, 298, 416
Peterson J. R., Fabian A. C., 2006, Phys. Rep., 427, 1
Peterson J. R., Kahn S. M., Paerels F. B. S., Kaastra J. S., Tamura T., Bleeker J. A. M., Ferrigno C., Jernigan J. G., 2003, ApJ, 590, 207
Pettini M., Shapley A. E., Steidel C. C., Cuby J.-G., Dickinson M., Moorwood A. F. M., Adelberger K. L., Giavalisco M., 2001, ApJ, 554, 981
Pipino A., Kaviraj S., Bildfell C., Babul A., Hoekstra H., Silk J., 2009, MNRAS, 395, 462
Piqueras L., Conseil S., Shepherd M., Bacon R., Leclercq F., Richard J., 2017, preprint (arXiv:1710.03554)
Pizzolato F., Soker N., 2005, ApJ, 632, 821
Postman M. et al., 2012, ApJS, 199, 25
Proxauf B., Öttl S., Kimeswenger S., 2014, A&A, 561, A10
Prugniel P., Soubiran C., Koleva M., Le Borgne D., 2007, preprint (arXiv:astro-ph/0703658)
Rawle T. D. et al., 2012, ApJ, 747, 29
Rieke G. H., Alonso-Herrero A., Weiner B. J., Pérez-González P. G., Blaylock M., Donley J. L., Marcillac D., 2009, ApJ, 692, 556
Rizza E., Burns J. O., Ledlow M. J., Owen F. N., Voges W., Bliton M., 1998, MNRAS, 301, 328
Rodríguez-Merino L. H., Chavez M., Bertone E., Buzzoni A., 2005, ApJ, 626, 411
Russell H. R., McNamara B. R., Edge A. C., Hogan M. T., Main R. A., Vantyghem A. N., 2013, MNRAS, 432, 530
Salomé P., Combes F., 2003, A&A, 412, 657
Salpeter E. E., 1955, ApJ, 121, 161
Saxton C. J., Bicknell G. V., Sutherland R. S., Midgley S., 2005, MNRAS, 359, 781
Schombert J. M., 1986, ApJS, 60, 603
Sérsic J. L., 1968, Atlas de Galaxias Australes. Observatorio Astronomico, Cordoba, Argentina
Sharma P., McCourt M., Quataert E., Parrish I. J., 2012, MNRAS, 420, 3174
Silk J., 1976, ApJ, 208, 646
Smolčić V., 2009, ApJ, 699, L43
Soto K. T., Lilly S. J., Bacon R., Richard J., Conseil S., 2016, MNRAS, 458, 3210
Storey P. J., Zeippen C. J., 2000, MNRAS, 312, 813
Stott J. P. et al., 2010, ApJ, 718, 23
Sun M., 2009, ApJ, 704, 1586
Tonini C., Bernyk M., Croton D., Maraston C., Thomas D., 2012, ApJ, 759, 43
Tremaine S. D., Richstone D. O., 1977, ApJ, 212, 311
Tremblay G. R. et al., 2016, Nature, 534, 218
Tremblay G. R. et al., 2018, ApJ, 865, 13
Veale M., Ma C.-P., Greene J. E., Thomas J., Blakeslee J. P., Walsh J. L., Ito J., 2018, MNRAS, 473, 5446
Veilleux S., Osterbrock D. E., 1987, ApJS, 63, 295
Venturi G. et al., 2018, A&A, 619, A74
Vika M., Bamford S. P., Häußler B., Rojas A. L., Borch A., Nichol R. C., 2013, MNRAS, 435, 623
Voigt L. M., Fabian A. C., 2004, MNRAS, 347, 1130
Voit G. M., Donahue M., Bryan G. L., McDonald M., 2015a, Nature, 519, 203
Voit G. M., Bryan G. L., O'Shea B. W., Donahue M., 2015b, ApJ, 808, L30
Von Der Linden A., Best P. N., Kauffmann G., White S. D. M., 2007, MNRAS, 379, 867
Vulcani B. et al., 2016, ApJ, 816, 86
Webb T. M. A. et al., 2015, ApJ, 814, 96
Weilbacher P. M., Streicher O., Urrutia T., Pécontal-Rousset A., Jarno A., Bacon R., 2014, in Manset N., Forshay P., eds, ASP Conf. Ser. Vol. 485, Astronomical Data Analysis Software and Systems XXIII. Astron. Soc. Pac., San Francisco, p. 451
White D. A., Jones C., Forman W., 1997, MNRAS, 292, 419
White S. D. M., 1976, MNRAS, 177, 717
Yang L., Tozzi P., Yu H., Lusso E., Gaspari M., Gilli R., Nardini E., Risaliti G., 2018, ApJ, 859, 65
Yu H. et al., 2018, ApJ, 853, 100
Zhao D., Aragón-Salamanca A., Conselice C. J., 2015, MNRAS, 453, 4444
Zubovas K., King A. R., 2012, MNRAS, 426, 2751

Downloaded from https://academic.oup.com/mnras/article/487/4/5593/5514359 by guest on 26 November 2020

APPENDIX A: ABELL 2667 BCG SURFACE BRIGHTNESS RADIAL PROFILE

In Fig. A1 we present the 1D radial profile of the observed Abell 2667 BCG surface brightness as extracted from the *HST* F814W-band image. We also show the best-matching GALFITM components for the sky background, intracluster light, and galaxy emission (i.e. Sérsic profile). Details of the fitting procedure are presented in Section 3.1.

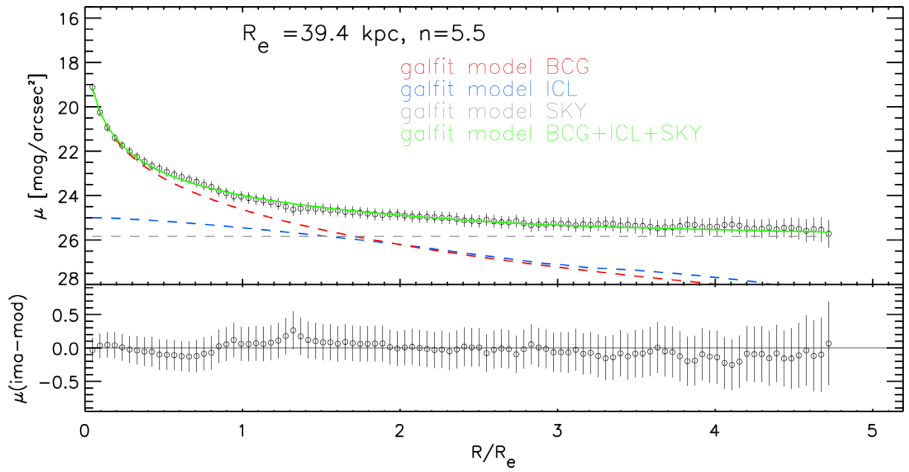


Figure A1. GALFITM fit (*green solid line*) of the BCG surface brightness profile in the F814W filter. The dashed lines highlight the best-matching radial profiles for the sky background (*grey line*), the ICL (*blue line*), and the central galaxy (*red line*).

APPENDIX B: MUSE INTEGRATED SPECTRUM OF ABELL 2667 BCG

In Fig. B1 we show the MUSE integrated spectrum of the Abell 2667 BCG. We also present the stellar continuum reconstructed by SINOPSIS and the residuals between the observed spectrum and the model.

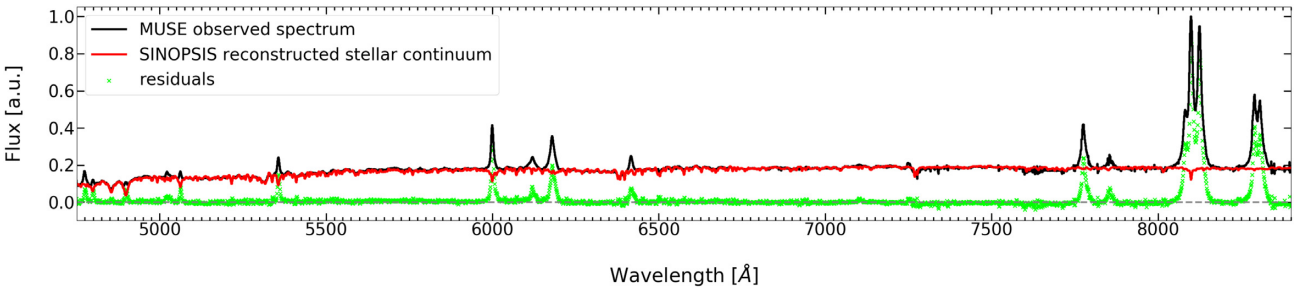


Figure B1. Example of a MUSE observed spectrum (*black solid line*) and its SINOPSIS reconstructed stellar continuum (*red solid line*) of the Abell 2667 BCG. The green crosses show the residuals between the observed and reconstructed model, i.e. the spectrum of only emission lines that we use for the analysis of the gas component in Section 3.3.

APPENDIX C: DETECTION OF A LY α-EMITTER CANDIDATE

In Fig. C1 we present wavelength cut-outs of the MUSE integrated spectrum for the Ly α-emitter candidate at $z \sim 4.08$ (see Section 3.3.1).

Downloaded from https://academic.oup.com/mnras/article/487/4/5593/5514359 by guest on 26 November 2020

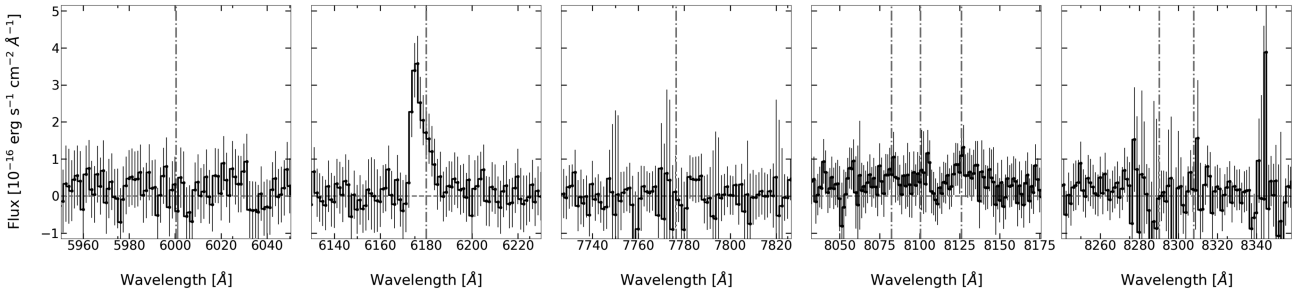


Figure C1. Integrated spectrum of the Ly α-emitter candidate at $z \sim 4.08$ (F region; see Fig. 7). We present wavelength cut-outs of the MUSE observed spectrum (*grey solid line*) and its 3σ error, integrated over a 1.2 arcsec $\times$ 1.2 arcsec region centred at RA (J2000.0) $= 23^{\rm h}51^{\rm m}39\overset{\rm s}{.}507$, Dec (J2000.0)$=-26^{\circ}04'56\overset{''}{.}81$. In the cut-outs, the vertical dash–dotted lines indicate the expected wavelength of H β, [O III] λ5007, [OI] λ6300, H α + [N II], and the [S II] doublet at the BCG redshift. The only line we detect falls in the [O III] λ5007 cut-out. However, the absence of the weaker component of the [O III] doublet and of the other lines, together with the highly asymmetric shape of the emission, suggests that the detection corresponds to a different line, possibly a Ly α.

[1]*Dipartimento di Fisica ed Astronomia, Università degli Studi di Padova, Vicolo dell'Osservatorio 3, I-35122 Padova, Italy*
[2]*European Southern Observatory, Karl Schwarzschild Straße 2, D-85748 Garching, Germany*
[3]*INAF – Osservatorio Astronomico di Padova, Vicolo dell'Osservatorio 5, I-35122 Padova, Italy*
[4]*Instituto de Radioastronomía y Astrofísica, UNAM, Campus Morelia, A.P. 3-72, C.P. 58089 Morelia, Mexico*
[5]*INAF – Osservatorio Astrofisico di Arcetri, Largo Enrico Fermi 5, I-50125 Firenze, Italy*
[6]*Dipartimento di Fisica e Scienze della Terra, Università degli Studi di Ferrara, Via Saragat 1, I-44122 Ferrara, Italy*
[7]*Kapteyn Astronomical Institute, University of Groningen, Postbus 800, NL-9700 AV Groningen, the Netherlands*
[8]*Institut de Radioastronomie Millimétrique 300 rue de la Piscine, Domaine Universitaire, F-38406 Saint Martin d'Hères, France*
[9]*Excellence Cluster Universe, Boltzmannstraße 2, D-85748 Garching, Germany*
[10]*SOFIA Science Center, USRA, NASA Ames Research Center, M.S. N232-12, Moffett Field, CA 9403, USA*
[11]*INAF – Osservatorio Astronomico di Capodimonte, via Moiariello 16, I-80131 Napoli, Italy*
[12]*Departamento de Astronomía y Astrofísica, Universidad Complutense de Madrid, Av. Complutense s/n, C.P. E-28040 Madrid, Spain*
[13]*Centro de Astrobiología (CAB, INTA-CSIC), Carretera de Ajalvir km 4, E-28850 Torrejón de Ardoz, Madrid, Spain*
[14]*Dipartimento di Fisica e Astronomia, Università degli Studi di Bologna, via Gobetti 93/2, I-40129 Bologna, Italy*
[15]*INAF – Istituto di Radioastronomia – Italian node of the ALMA Regional Centre (ARC), via Gobetti 101, I-40129 Bologna, Italy*
[16]*Departamento de Astronomía, Universidad de Concepción, Barrio Universitario, 4030000 Concepción, Chile*
[17]*Leiden Observatory, Leiden University, PO Box 9513, NL-2300 RA Leiden, the Netherlands*

This paper has been typeset from a TEX/LATEX file prepared by the author.

Downloaded from https://academic.oup.com/mnras/article/487/4/5593/5514359 by guest on 26 November 2020